Alma Mater Studiorum Università di Bologna
Archivio istituzionale della ricerca

Dimensionless fluid-to-ground thermal response of single-line bore fields with isothermal fluid

27 July 2024

Dimensionless fluid-to-ground thermal response of single-line bore fields with isothermal fluid

Enzo Zanchini[*], Claudia Naldi, Matteo Dongellini

Department of Industrial Engineering (DIN), Alma Mater Studiorum University of Bologna, Viale Risorgimento 2, 40136 Bologna, Italy

[*]Corresponding author: enzo.zanchini@unibo.it

Abstract

The design of a borehole-heat-exchanger (BHE) field is usually performed by means of dimensionless functions, called *g-functions*, that yield the time evolution of the mean temperature of the external surface of the BHEs, T_{sm}, produced by a time constant heat flux, which is usually considered as uniform. The mean temperature of the fluid, T_{fm}, is then evaluated by adding to T_{sm} the product of the heat flux per unit length and the BHE thermal resistance. This method overestimates the difference between T_{fm} and T_{sm} in the short term, and overestimates the *g-function* of the field in the long term. Methods to obtain more accurate results have been proposed, but require difficult and time-consuming numerical computations. In this paper dimensionless *fluid-to-ground* (*ftg*) *functions* that yield directly the time evolution of T_{fm}, in a time scale from a few minutes to hundreds of years, are provided for any single-line bore field subjected to a time constant heat flux, composed of up to four BHEs fed in parallel with the same inlet temperature. The *ftg-functions* are obtained by finite-element simulations implemented in COMSOL Multiphysics, and are reported in two Excel files that, after entering the dimensionless parameters of the BHE field under examination, instantly yield a short-term and a long-term *ftg-function* perfectly joined at the separation instant. The main novelties of this work are the characterization of each BHE field by a few dimensionless parameters, the improvement of the BHE model presented in Naldi and Zanchini 2020, the accuracy, speed and simplicity of use of the final results. The validations of the simulation codes for a single BHE and for fields of 3 and 4 BHEs, by comparison with analytical solutions, yielded root-mean-square deviations equal to 0.023%, 0.43%, and 0.49% of the mean value, respectively. The validation of the simulation code for two BHEs, performed with an extremely high distance between the BHEs, yielded a root-mean-square deviation equal to 0.054 % of the mean value, with respect to the long-term *ftg-function* obtained for a single BHE.

Keywords

Ground-coupled heat pumps; Borehole heat exchangers; Fluid-to-ground thermal response factors; Single-line bore fields; Isothermal fluid; Finite-element simulations.

Nomenclature

a	Rescaling coefficient, interpolation parameter	
b	Interpolation parameter	
B_d	Buried depth	(m)
BHE	Borehole Heat Exchanger	
c_1, c_2	Correction coefficients, defined in Eqs. (24), (25)	
d	Spacing between boreholes	(m)
Ei	Exponential integral function	
Erf	Error function, defined in Eq. (29)	
FLS	Finite line-source	
ftg	Fluid-to-ground	
GCHP	Ground-coupled heat pump	
H	Borehole length	(m)
HC_L	Heat capacity per unit length	$(J\ m^{-1}\ K^{-1})$
Ierf	Integral error function, defined in Eq. (28)	
I_{LS}	Function defined in Eq. (27)	$(W\ m^{-1}\ K^{-1})$
k	Thermal conductivity	
OMEC	One-Material Equivalent Cylinder	
Q	Total heat flux	(W)
q_l	Heat flux per unit length	$(W\ m^{-1})$
r	Radius, radial coordinate	(m)
R_b	Borehole thermal resistance per unit length	$(m\ K\ W^{-1})$
s	Shank spacing	(m)
T	Temperature	(°C)
$TRCMs$	Thermal resistance and capacity models	
x, y	Horizontal coordinates	(m)
z	Vertical coordinate	(m)

Greek symbols

θ	Temperature difference	(°C)

$(\rho\, c)$	Volumetric heat capacity	$(\mathrm{J\ m^{-3}\ K^{-1}})$
τ	Time	(s)
τ_0	Instant of time	(s)
φ	Dimensionless coefficient	
ϕ	Angular coordinate	rad

Superscripts

*	Dimensionless

Subscripts

b	Of borehole
e	External
eff	Effective
eq	Equivalent
fm	Mean, of fluid
g	Of the ground
gt	Of the grout
i	Internal
p	Of pipe
r	rescaled
sc	Of the superconductor
sm	Mean, of surface

1. Introduction

Ground-Coupled Heat Pumps (GCHPs) are the most efficient and eco-friendly system for air conditioning, in both winter and summer [1, 2]. In most applications, GCHPs are equipped with vertical ground heat exchangers, called Borehole Heat Exchangers (BHEs), having a diameter of about 15 cm and a typical length between 60 and 150 m. Each BHE is usually composed of either a single U-tube or a double U-tube in high density polyethylene, surrounded by a sealing grout.

The most accurate methods for the design and the simulation of a BHE field are based on functions called thermal response factors. A thermal response factor yields the time evolution of either the mean temperature of the surface between BHEs and ground, T_{sm}, or the mean temperature of the fluid in the BHEs, T_{fm}, produced by a time constant heat flux from the BHEs to the ground. In this paper, a dimensionless thermal response factor yielding the time evolution of T_{sm} is called *g-function*, and a dimensionless thermal response factor yielding the time evolution of T_{fm} is called fluid-to-ground

function (*ftg-function*). In the long term, *g-functions* and *ftg-functions* can be considered as equivalent, because the heat transfer inside the BHEs is quasi-stationary and the difference between T_{fm} and T_{sm} is given by

$$T_{fm} - T_{sm} = q_l R_b \quad , \tag{1}$$

where q_l is the mean heat flux per unit length from the BHEs to the ground and R_b is the BHE thermal resistance, that can be evaluated by a numerical simulation of a BHE cross section or by a thermal response test (TRT). On the contrary, *g-functions* do not determine accurately T_{fm} in the short time, when Eq. (1) does not hold.

Under the assumption of uniform heat flux, the *g-function* for a single BHE can be easily calculated by the Finite Line-Source (FLS) scheme, that sketches the BHE as line with a finite length H, having its top at a buried depth B_d beneath the ground surface. Analytical expressions of the temperature field produced by a FLS with $B_d = 0$ were determined by Zeng et al. [3], and, in simpler forms, by Lamarche and Beauchamp [4] and by Bandos et al. [5]. An analytical solution for the general case $B_d \neq 0$ was obtained by Claesson and Javed [6]. Under the same assumption, the *g-function* of a BHE field can be evaluated by the superposition of the effects of the single BHEs, so that it is not necessary to perform a computation for each field.

In real applications, however, the BHEs of a field are fed in parallel with the same inlet temperature and the heat flux is not quite uniform along each BHE and is not the same for all BHEs. Therefore, Eskilson [7] preferred to consider the boundary condition of time constant total heat flux and uniform temperature of the bore field surface, and determined numerically the *g-functions* of several BHE fields under this condition. A semi-analytical method to determine *g-functions* with Eskilson's boundary condition was proposed by Cimmino and Bernier [8]. These authors showed that, in the case of large BHE fields with compact shape, the *g-functions* evaluated by the FLS scheme with uniform heat flux overestimate considerably the ground thermal response, with respect to Eskilson's *g-functions*. Improvements of the method presented in Ref. [8], with the aim of reducing the computation time, were proposed by Lamarche [9] and by Cimmino [10]. Numerical methods to determine *g-functions* with the boundary condition of uniform surface temperature of the BHE field were proposed by Monzó et al. [11] and by Naldi and Zanchini [12].

Indeed, while the fluid temperature averaged between the pipes is almost independent of the vertical coordinate, z, the surface temperature of the BHEs varies with z, due to the combined effect of the BHE thermal resistance and the non-uniform heat flux per unit length. As a consequence, the condition of uniform temperature should be imposed on the boundary between the working fluid and the pipes, and not at the external surface of the BHEs. Monzó et al. [13] refined the numerical method of Ref. [11] to take into account the effects of the BHE thermal resistance. Cimmino [14] improved

the method employed in Ref. [8] in order to obtain *g-functions* with the boundary condition of equal inlet fluid temperature for all boreholes in the field.

Even if evaluated with the most suitable boundary conditions, namely time constant total heat flux and either uniform fluid temperature or equal intel temperature for all the BHEs, *g-functions* are not completely satisfactory because they do not yield accurately the time evolution of the mean fluid temperature in the short time. Therefore, several authors developed methods to determine *ftg-functions*, suitable to determine the effects of peak loads on the mean fluid temperature.

Some methods to determine the short-term thermal response of a BHE are based on representing the BHE by a grid of thermal resistances and heat capacities, and are called thermal resistance and capacity models (TRCMs). Methods of this kind were proposed by De Carli et al. [15], Zarrella et al. [16], Bauer et al. [17], Pasquier and Marcotte [18], Ruiz-Calvo et al. [19]. Other analytical or numerical BHE models are based on replacing the pipes by a single equivalent pipe coaxial with the BHE axis, so that the BHE geometry becomes axisymmetric. Models of this kind were proposed by Gu and O'Neal [20], Shonder and Beck [21], Beier and Smith [22], Xu and Spitler [23], Lamarche and Beauchamp [24], Bandyopadhyay et al. [25, 26], Man et al. [27], Javed and Claesson [28], Lamarche [29], Naldi and Zanchini [30]. Three of these models will be briefly illustrated: the model presented in Ref. [27], that will be employed for a validation of our 2D axisymmetric simulation code, the model developed in Ref. [29], that is very accurate, and that proposed in Ref. [30], that will be employed, with a slight modification, to determine our *ftg-functions*.

In the model of Man et al. [27], the BHE is represented by a solid cylinder with the same thermal properties as the external ground, containing a heat-generating cylindrical surface that represents the heat supplied by the fluid. The authors provide two analytical solutions for the model: the first solution is for the case of purely radial heat flow, while the second is for 2D axisymmetric heat flow and takes into account the finite BHE length. The analytical solutions contain an integral that must be computed numerically, but the numerical computation is rather simple and can be performed with high accuracy. The solution for purely radial heat flow is employed in this paper to validate the finite-element simulation code of our new cylindrical model, in the special case of purely radial heat flow and properties of the model equal to those of the ground.

In Lamarche [29], the fluid is modeled as an isothermal cylinder with a heat capacity per unit length equal to that of the real fluid, surrounded by a thin cylindrical resistive layer with a thermal resistance per unit length equal to that between fluid and grout, surrounded on turn by a cylindrical layer representing the grout, with external radius equal to that of the BHE. The fluid is subjected to a given heat generation per unit time and unit BHE length. The external radius of the resistive layer is selected to reproduce the grout thermal resistance with the real grout thermal conductivity, and the volumetric

heat capacity of the grout is adjusted to yield the real heat capacity per unit length. The author determined an analytical solution for his model and found a good agreement between his results and those obtained by Beier and Smith [22] and by Javed and Claesson [28]. The excellent accuracy of a numerical version of the model proposed by Lamarche [29] was proved in Ref. [30].

In the model proposed in Ref. [30], called One Material Equivalent Cylinder (OMEC), the BHE is represented by an equivalent solid cylinder made of one material, with the same radius as the BHE, r_b. The OMEC contains a heat-generating cylindrical surface, with radius r_{eq}, that replaces the BHE fluid. The thermal conductivity and the volumetric heat capacity of the OMEC are chosen so that the thermal resistance of the cylindrical annulus between r_{eq} and r_b is equal to the BHE thermal resistance, and the heat capacity per unit length of the OMEC is equal to that of the BHE. The optimal value of r_{eq} can be determined by repeated 2D numerical simulations. A table and a correlation that yield the optimal value of r_{eq} for single U-tube BHEs is reported in Ref. [30]. In this paper, a slight modification of the model is adopted, that will be illustrated in Section 2. In the modified form, the cylindrical model is as accurate as the model by Lamarche [29], and has the advantage of being determined by a lower number of parameters.

In order to perform a careful design or an accurate simulation of a BHE field, one needs a *ftg-function* valid in the full-time scale, from some minutes to many years. Some methods to determine full-time-scale *ftg-functions* have been proposed in the literature. Claesson and Javed [6] proposed to employ their axisymmetric BHE model [28] for the short-term analysis, and their analytical solution of the FLS model with uniform heat flux [6], coupled with the superposition of the effects of single BHEs, for the long-term analysis. The authors suggested a method for matching the short-term and the long-term solution. However, the FLS model with uniform heat flux does not yield accurate *ftg-functions* for BHE fields in the long term. Naldi and Zanchini [31] showed that their OMEC model [30] can be used to obtain accurate *ftg-functions* for BHE fields with uniform fluid temperature and presented the simulation results for a square field of 4 BHEs. Laferrière et al. [32] developed a full-time-scale bore field simulation model, where a semi-analytical tool yielding the *g-function* for a BHE field with the boundary condition of uniform bore-field surface temperature is coupled with a thermal resistances and capacities model that yields the time evolution of the fluid temperature in short time scales.

Although methods for determining full-time-scale *ftg-functions* of bore fields are available, the use of these methods requires a high-level and time-consuming computational work. Therefore, dimensionless results easily employable to determine the *ftg-function* of any bore field with a usual geometry would be useful for designers.

In this paper the full-time-scale *ftg-functions* are provided for single-line bore fields with up to 4 BHEs and isothermal fluid. The result is obtained through a BHE model that allows characterizing a

BHE field by six dimensionless parameters, and finite-element simulations implemented in COMSOL Multiphysics. Each BHE is modeled as a solid cylinder, with radius equal to the BHE radius and a uniform volumetric heat capacity, composed of a superconductive inner core and an annulus with a thermal conductivity such that the thermal resistance of the annulus is equal to the BHE thermal resistance.

One of the dimensionless parameters, namely the dimensionless buried depth, is kept fixed. Three values are considered for each variable parameter. The number of combinations is reduced by proving that only 3 variable parameters have appreciable effects on the short-term *ftg-functions*, and only 3 (2 in the case of a single BHE) have appreciable effects on the long-term *ftg-functions*. For BHE fields with two or more BHEs, the condition of equal temperatures of the superconductive cores is ensured by a superconductive horizontal bar that interconnects them.

The final product consists of two Excel files that, after entering the dimensionless parameters that characterize any single-line BHE field with up to 4 BHEs, instantly yield a short-term and a long-term *ftg-function* perfectly joined at the separation instant. Thus, unlike most of the available numerical and semi-analytical methods, that are difficult to apply and time consuming, the results provided in this paper are very easy to employ, and can be highly useful in standard design and simulation activities.

The results apply to single U-tube and double U-tube BHEs, with ratios between length and radius from 800 to 2000, i.e., length between 60 and 150 m for r_b =7.5 cm, in the absence of appreciable effects of groundwater seepage. The effects of groundwater seepage and the extension to other common bore-field geometries will be considered in future work.

2. Mathematical model

The ground is modeled as a homogeneous solid, equivalent to the real sequence of soil layers. This scheme, usually adopted, has been proved to be sufficiently accurate [33, 34]. The BHE model employed is a slight modification of the OMEC model presented in Ref. [30]. Each BHE is modeled as a one-material cylindrical annulus, with radius r_b, containing a superconductive inner core with radius r_{eq} and the same volumetric heat capacity as the annulus. The thermal conductivity of the cylindrical annulus, k_{eq}, and the volumetric heat capacity of both the inner core and the annulus, $(\rho c)_{eq}$, are such that the thermal resistance of the annulus is equal to R_b, and the heat capacity of the cylindrical model is equal to that of the BHE. The thermal conductivity of the superconductor is chosen so high that increasing or decreasing its value by an order of magnitude has no effect on the *ftg-function*. The superconductive core is subjected to a heat flux Q at its top surface. For single U-tube BHEs, the optimal value of r_{eq} can be taken from the table or from the correlation reported in

Ref. [30]. For other kinds of BHEs, the optimal value of r_{eq} can be determined by repeated simulations of a BHE cross section.

An example of the model is illustrated in Figure 1. In the real BHE cross section, that appears on the left, the grout is in light brown, the pipes are in grey, and the water is in blue. In the cylindrical model, that appears on the right, the superconductive core is in blue and the annulus is in light grey. The geometry is specified in the figure, with lengths in cm. The thermal conductivity of the grout is $k_{gt} = 1.6$ W/(mK), that of the ground is $k_g = 1.8$ W/(mK), and the volumetric heat capacities of the grout and of the ground are equal, with values $(\rho c)_{gt} = (\rho c)_g = 3.0$ MJ/(m³K). The corresponding radius of the superconductive core is $r_{eq} = 2.16$ cm, as reported in Table 2 of Ref. [30]. A complete set of data is reported in Section 2, where this example is used to check the accuracy of the model.
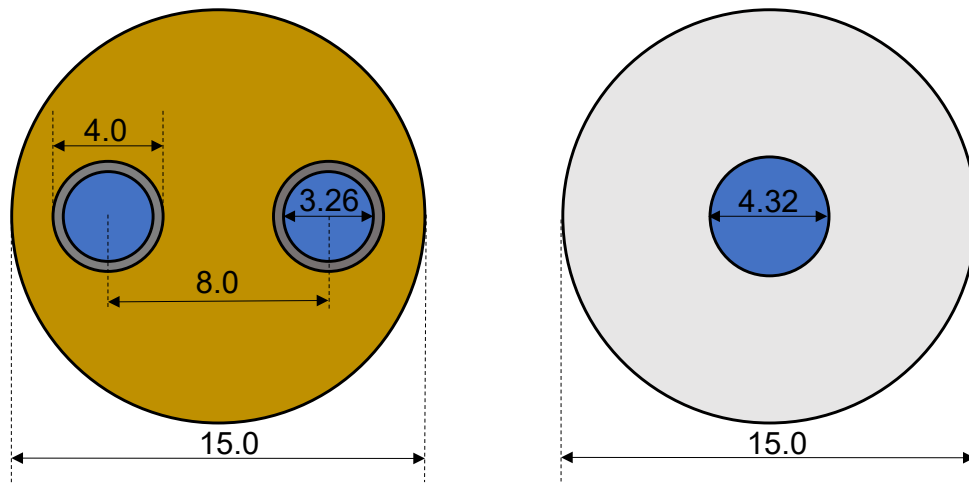

Figure 1. Cross section of a single U-tube BHE (left) and of the corresponding cylindrical model with superconductive core (right), with lengths in cm.

In the case of a BHE field, all the top surfaces of the BHEs are connected by a superconductive bar that is subjected to the total heat flux of the bore field. The mean temperature of the superconductive inner core of the BHEs represents the mean fluid temperature. The new cylindrical model has been preferred to the original OMEC model [30], employed in Ref. [31], to avoid the repeated simulations that are necessary to reach the condition of uniform fluid temperature with that model. For single U-tube BHEs, the optimal values of r_{eq} reported in Ref. [30] can be adopted without changes, and the new model is more precise than the original one.

Our model, like any other purely conductive model, does not simulate the fluid flow. Therefore, the *ftg-functions* determined by our model could be not accurate for values of time lower than the time employed by the fluid to travel a complete path through the borehole. Another potential cause of inaccuracy could be the fact that our model does not consider the thermal short-circuiting between the legs of the BHE. However, as is shown in Ref. [35], the temperature distribution along the flow

direction has a negligible effect on the borehole thermal resistance. As a consequence, a negligible effect of the thermal short-circuiting in the time evolution of the mean fluid temperature is expected. On the contrary, the thermal short-circuiting may have a relevant effect on the difference between the outlet temperature and the mean temperature of the fluid, for long BHEs and low flow rates. This difference can be easily determined by employing Eq. (6) of Ref. [36], with the values of the dimensionless coefficient φ given in Ref. [36] for single U-tube BHEs and in Ref. [37] for double U-tube BHEs.

2.1. Differential equations and limit conditions

For a single BHE, the local energy balance equations in the superconductive core, in the cylindrical annulus surrounding the core and in the ground are given by equations (2), (3), (4), respectively:

$$\frac{\partial T}{\partial \tau} = \frac{k_{sc}}{(\rho c)_{eq}} \nabla^2 T, \quad 0 \le r \le r_{eq}, -H \le z \le 0 \,, \tag{2}$$

$$\frac{\partial T}{\partial \tau} = \frac{k_{eq}}{(\rho c)_{eq}} \nabla^2 T, \quad r_{eq} \le r \le r_b, -H \le z \le 0 \quad, \tag{3}$$

$$\frac{\partial T}{\partial \tau} = \frac{k_g}{(\rho c)_g} \nabla^2 T, \quad r \ge r_b \,. \tag{4}$$

In Eqs. (2) – (4), T is temperature; τ is time; r is the radial coordinate; z is the vertical coordinate, with origin at the top of the BHE; H is the BHE length; k_{sc}, k_{eq}, and k_g are the thermal conductivities of the superconductor, of the cylindrical annulus and of the ground; $(\rho c)_{eq}$ and $(\rho c)_g$ are the volumetric heat capacities of the whole cylindrical model and of the ground.

The initial condition, in the whole computational domain, is

$$T(r, z, 0) = T_g \quad, \tag{5}$$

where T_g is the undisturbed ground temperature, assumed to be uniform. The boundary condition at the ground surface, placed at $z = B_d$, is

$$T(r, B_d, \tau) = T_g \quad. \tag{6}$$

The conditions at the internal boundaries between superconductor and cylindrical annulus and between annulus and ground are the continuity of temperature and

$$-k_{sc} \left.\frac{\partial T}{\partial r}\right|^-_{r=r_{eq}} = -k_{eq} \left.\frac{\partial T}{\partial r}\right|^+_{r=r_{eq}}, \quad -H \le z \le 0 \quad, \tag{7}$$

$$-k_{eq} \left.\frac{\partial T}{\partial r}\right|^-_{r=r_b} = -k_g \left.\frac{\partial T}{\partial r}\right|^+_{r=r_b}, \quad -H \le z \le 0 \quad. \tag{8}$$

The boundary condition at the superconductor upper surface is

$$k_{sc} \frac{\partial T}{\partial z}\bigg|_{z=0} = \frac{Q}{\pi r_{eq}^2}, \quad z = 0, \ 0 \le r \le r_{eq} \ , \tag{9}$$

where Q is the heat flux supplied to the BHE. All the other boundaries are adiabatic.

2.2 Dimensionless quantities, dimensionless differential equations and limit conditions

The dimensionless temperature, T^*, the dimensionless time, τ^*, the dimensionless Nabla operator, ∇^*, the dimensionless coordinates, r^* and z^*, the dimensionless thermal conductivities of the superconductor and of the cylindrical annulus, k_{sc}^* and k_{eq}^*, and the dimensionless volumetric heat capacity of the whole cylindrical model, $(\rho c)_{eq}^*$, are defined as follows:

$$T^* = \frac{k_g H \left(T - T_g \right)}{Q}; \quad \tau^* = \frac{k_g \tau}{\left(\rho c \right)_g r_b^2}; \quad \nabla^* = r_b \nabla; \quad r^* = \frac{r}{r_b}; \quad r_{eq}^* = \frac{r_{eq}}{r_b};$$

$$z^* = \frac{z}{r_b}; \quad H^* = \frac{H}{r_b}; \quad k_{sc}^* = \frac{k_{sc}}{k_g}; \quad k_{eq}^* = \frac{k_{eq}}{k_g}; \quad \left(\rho c \right)_{eq}^* = \frac{\left(\rho c \right)_{eq}}{\left(\rho c \right)_g} \tag{10}$$

By introducing in Eqs. (2) – (9) the dimensionless quantities defined above, one obtains the following dimensionless differential equations and limit conditions

$$\frac{\partial T^*}{\partial \tau^*} = \frac{k_{sc}^*}{\left(\rho c \right)_{eq}^*} \nabla^{*2} T^*, \quad 0 \le r^* \le r_{eq}^*, -H^* \le z^* \le 0 \ , \tag{11}$$

$$\frac{\partial T^*}{\partial \tau^*} = \frac{k_{eq}^*}{\left(\rho c \right)_{eq}^*} \nabla^{*2} T^*, \quad r_{eq}^* \le r^* \le 1, -H^* \le z^* \le 0 \ , \tag{12}$$

$$\frac{\partial T^*}{\partial \tau^*} = \nabla^{*2} T^*, \quad r^* \ge 1 \ , \tag{13}$$

$$T^* \left(r^*, z^*, 0 \right) = 0 \ , \tag{14}$$

$$T^* \left(r^*, B_d^*, \tau^* \right) = 0 \ , \tag{15}$$

$$-k_{sc}^* \frac{\partial T^*}{\partial r^*}\bigg|_{r^*=r_{eq}^*}^{-} = -k_{eq}^* \frac{\partial T^*}{\partial r^*}\bigg|_{r^*=r_{eq}^*}^{+}, \quad -H^* \le z^* \le 0 \ , \tag{16}$$

$$-k_{eq}^* \frac{\partial T^*}{\partial r^*}\bigg|_{r^*=1}^{-} = -\frac{\partial T^*}{\partial r^*}\bigg|_{r^*=1}^{+}, \quad -H^* \le z^* \le 0 \ , \tag{17}$$

$$k_{sc}^* \frac{\partial T^*}{\partial z^*}\bigg|_{z^*=0}^{-} = \frac{H^*}{\pi r_{eq}^{*2}}, \quad z^* = 0, 0 \le r^* \le r_{eq}^* \ . \tag{18}$$

Since k_{sc} is chosen so high that the temperature distribution is independent of k_{sc}, Eqs. (11) – (18) show that the dimensionless temperature distribution $T^* \left(r^*, z^*, \tau^* \right)$ depends only on

$r_{eq}^*, H^*, B_d^*, (\rho c)_{eq}^*, k_{eq}^*$. The parameter B_d^* has not a strong effect on the result and is kept equal to 24, i.e. 1.80 m for radius 7.5 cm. Under this assumption, the dimensionless temperature field for a single BHE, in the cylindrical model, depends only on $r_{eq}^*, H^*, (\rho c)_{eq}^*, k_{eq}^*$. The parameter k_{eq}^* can be replaced by the dimensionless BHE thermal resistance, R_b^* . In fact, one has

$$R_b^* = k_g R_b = \frac{1}{2\pi k_{eq}^*} \ln \frac{1}{r_{eq}^*} \quad , \tag{19}$$

$$k_{eq}^* = \frac{1}{2\pi R_b^*} \ln \frac{1}{r_{eq}^*} \quad . \tag{20}$$

The *ftg-function* for a single BHE, i.e. the volume average of T^* on the superconductive core, is computed as a function of $R_b^*, r_{eq}^*, (\rho c)_{eq}^*, H^*$. The *ftg-function* for a single-line bore field with $n > 1$ BHEs is computed as a function of those parameters plus an additional one, namely the dimensionless spacing between adjacent BHEs,

$$d^* = \frac{d}{r_b} \quad . \tag{21}$$

2.3 Evaluation of the cross-section dimensionless parameters of the model

The evaluation of the cross-section dimensionless parameters of the model, R_b^*, r_{eq}^*, and $(\rho c)_{eq}^*$, requires the knowledge of the geometrical parameters of the BHE cross section and of the thermal properties of the ground and of the BHE materials. The equivalent thermal conductivity of the homogeneous soil that corresponds to the real sequence of soil layers can be determined accurately by a TRT evaluated with the usual Infinite Line-Source scheme, provided that the heat flux per unit length supplied to the BHE, q_l, is much greater than the product of the geothermal heat flux per unit area multiplied by the BHE length, H [38, 39]. For $H \leq 150$ m and typical values of the geothermal gradient, this condition is automatically fulfilled if the ASHRAE recommendations are followed. On the contrary, an accurate determination of the thermal conductivity of the grout, k_{gt}, and of the volumetric heat capacities of the grout and of the ground, $(\rho c)_{gt}$ and $(\rho c)_g$, is more problematic and requires a numerical evaluation of a TRT. Indeed, the values of k_{gt} and $(\rho c)_{gt}$ given by the manufacturer, or obtained by laboratory measurements, often do not correspond to those of the material in the real conditions taking place in the BHE [40].

A flow chart illustrating the evaluation of the cross-section dimensionless parameters of the model is reported in Figure 2. For single U-tube BHEs, the evaluation is very simple, because the optimal value of r_{eq}^* can be found in Ref. [30]. For double U-tube BHEs, the optimal value of r_{eq}^* must be

determined iteratively, by comparing the results of 2D short-term simulations of the cross sections of the BHE and of the model.
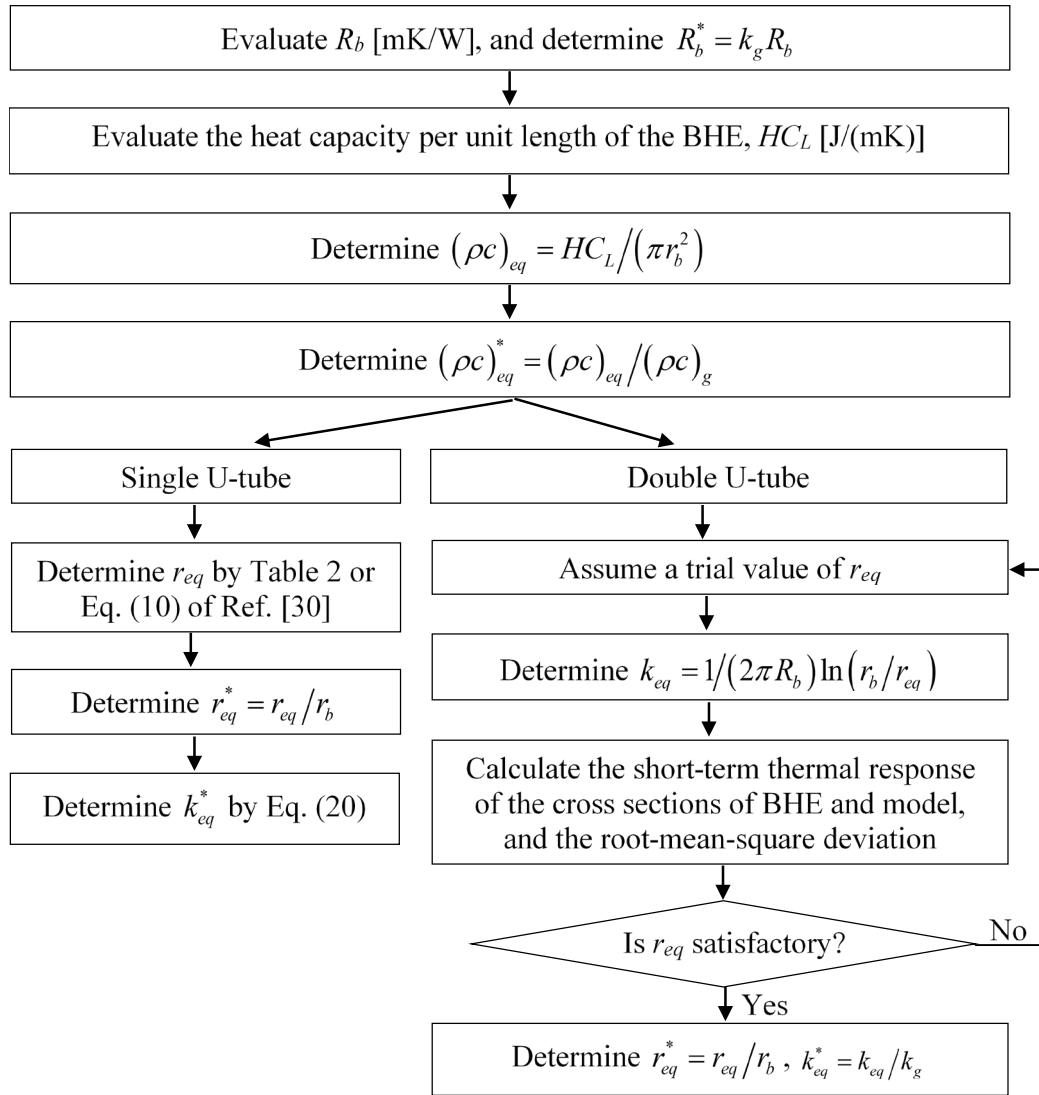

Figure 2. Flow chart illustrating the evaluation of the dimensionless parameters R_b^*, r_{eq}^*, and $\left(\rho c\right)_{eq}^*$ of the model

3. Validation of the model and of the simulation code

In this section, first the accuracy of the new cylindrical model is checked by comparison with a simulation of the real BHE, then the simulation code of the model is validated by comparison with the analytical model by Man et al. [27], in a special case.

3.1. Check of the accuracy of the cylindrical model

The accuracy of the model is checked by comparing the *ftg-function* obtained by a finite-element simulation of the model with that obtained by a finite-element simulation of the real BHE, in conditions of purely radial heat flux.

The simulation of the real BHE is performed by considering a BHE cross section surrounded by the ground, with reference to the single U-tube BHE illustrated in Figure 1. The thermal power per unit length supplied to the fluid, q_l = 50 W/m, is reproduced by a uniform heat generation term in a superconductive solid that represents the fluid [30, 41]. The convection coefficient between water and pipes is determined by the Churchill correlation [42] at constant heat flux, by considering a volume flow rate of 14 liters per minute and water properties evaluated at 20°C: density 998.21 kg/m^3, dynamic viscosity 0.0010016 Pa s, thermal conductivity 0.59846 W/(mK), specific heat capacity at constant pressure 4184.1 J/(kgK) [43]. The Reynolds number is 9082, the Nusselt number is 80.186, the convection coefficient is 1472 W/(m^{2}K). Since the fluid is replaced by a heat generating solid, the convective thermal resistance is included in the conductive thermal resistance of the pipes. For this purpose, the thermal conductivity of the pipes, k_p = 0.4 W/(mK), is replaced by an effective thermal conductivity, k_{peff} = 0.369859 W/(mK). The simulation is performed in dimensionless form, and is implemented in COMSOL Multiphysics. The dimensional quantities characterizing the BHE and the dimensionless quantities employed in the simulation are reported in Table 1. In order to obtain as output the dimensionless temperature field, the undisturbed ground temperature is replaced by T_g^* = 0, the ground thermal conductivity is replaced by k_g^* = 1, and the linear heat flux is replaced by q_l^* = 1.

The dimensionless-time interval considered in the simulation is $10^{-4} \leq \tau^* \leq 10^2$. For a ground thermal diffusivity equal to 7.5×10^{-7} m^2/s and r_b = 7.5 cm, it corresponds to the time interval $0.75 \text{ s} \leq \tau \leq 7.5 \times 10^5 \text{ s} \approx 208.33$ h. The computational domain is a circle having dimensionless radius 100 (7.5 m for r_b = 7.5 cm), center in the BHE axis, and adiabatic external boundary. The size of the computational domain is such that the effects of the boundary condition on the *ftg-function* are lower than 10^{-5}. This result has been checked by replacing the adiabatic boundary condition with that of uniform dimensionless temperature, T^* = 0. The mesh selected consists of 137720 triangular elements and is obtained by a regular refinement of the extremely fine physics-controlled mesh built by the software. Further mesh refinements do not yield significant changes of the *ftg-function*. A particular of the mesh, that shows a narrow region around the BHE, is illustrated in Figure 3. Values of the *ftg-function* are collected with steps of 0.05 in $\log_{10}(\tau^*)$. The time steps for the computation are selected by the software, in order to reach the accuracy parameters imposed: relative accuracy 0.0001 and absolute accuracy 0.0001.

The simulation of the cylindrical model is performed by a 2D axisymmetric code, that refers to a 105 m long BHE with cross section characterized by the parameters reported in Table 1. A heat flux Q = 5250 W is applied to the top of the superconductive core. In order to have purely radial heat flux in the whole domain surrounding the superconductive core, the buried depth is assumed as vanishing

and the computational domain is bounded by two adiabatic horizontal surfaces at $z = 0$ and at $z = -H$. The equivalent radius of the superconductive core is $r_{eq} = 2.16$ cm, as reported in Table 2 of Ref. [30] and illustrated in Figure 1.

Table 1. Dimensional quantities that characterize the BHE and corresponding dimensionless quantities employed in the 2D simulation of the BHE.

| Quantity	Dimensional quantities			Dimensionless quantities	
	Symbol	Unit	Value	Symbol	Value
Borehole radius	r_b	m	0.075	$r_b{}^*$	1
Pipe external radius	r_{pe}	m	0.02	$r_{pe}{}^*$	0.266667
Pipe internal radius	r_{pi}	m	0.0163	$r_{pe}{}^*$	0.217333
Shank spacing	s	m	0.08	s^*	1.066667
Linear heat flux	q_l	W/m	50	$q_l{}^*$	1
Heat generation	q_g	W/m³	29951.25	$q_g{}^*$	3.369515
Superconductor thermal conductivity	k_{sc}	W/(mK)	1.8×10^6	$k_{sc}{}^*$	10^6
Pipe effective thermal conductivity	k_{peff}	W/(mK)	0.369859	$k_{peff}{}^*$	0.205477
Grout thermal conductivity	k_{gt}	W/(mK)	1.6	$k_{gt}{}^*$	0.888889
Ground thermal conductivity	k_g	W/(mK)	1.8	$k_g{}^*$	1
Pipe volumetric heat capacity	$(\rho c)_p$	MJ/(m³K)	1.824	$(\rho c)_p{}^*$	0.608
Ground volumetric heat capacity	$(\rho c)_g$	MJ/(m³K)	3	$(\rho c)_g{}^*$	1
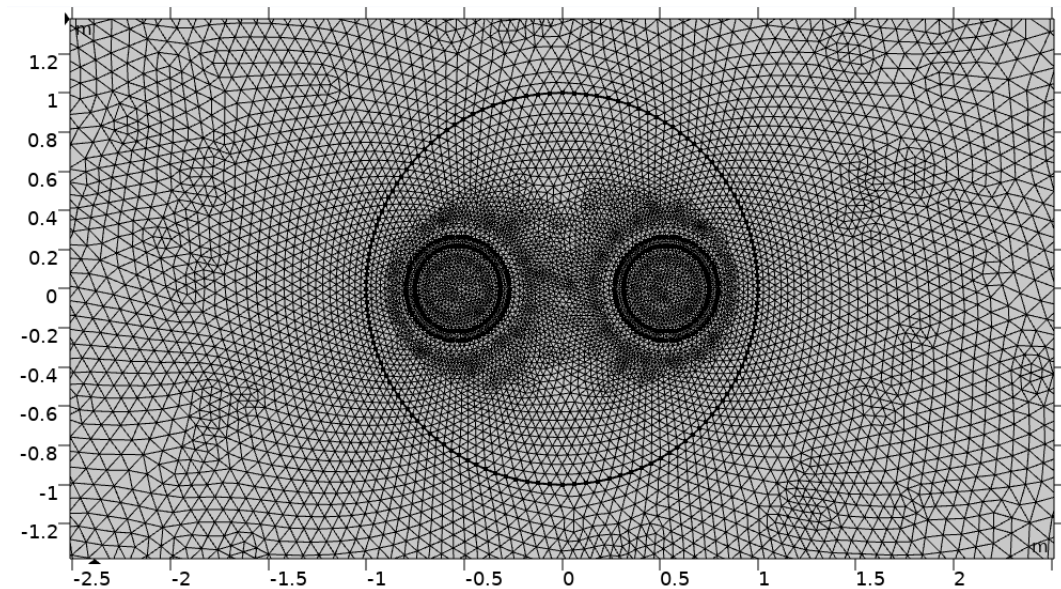
Figure 3. Particular of the triangular mesh employed in the 2D simulation of the real BHE.

In order to determine the equivalent thermal conductivity of the cylindrical annulus, k_{eq}, the BHE thermal resistance is calculated by a stationary 2D simulation of a BHE cross section surrounded by a ground layer with external radius 5 m. The fluid is replaced by two holes in the computational

domain, and a convective boundary condition is imposed at the internal surface of the pipes, with convection coefficient 1472 W/(m²K) and mean fluid temperature T_{fm} = 25 °C. A uniform temperature equal to 0 °C is imposed on the external boundary of the ground. The selected mesh has 132016 triangular elements, and is obtained by a regular refinement of extremely fine physics-controlled mesh built by the software. The relative accuracy is set equal to 0.00001. The results of the simulation are: T_{sm} = 19.444 °C, q_l = 52.363 W/m, and, from Eq. (1), R_b = 0.106105 mK/W. Thus, by applying the dimensional form of Eq. (19) one obtains k_{eq} = 1.86715 W/(mK), and, by Eq. (10), k_{eq}^* = 1.03731.

In analogy with previous papers [35 – 37, 41, 44], the vertical coordinate, z, is replaced by the rescaled one, $z_r = z/20$, in order to reduce the vertical length of the computational domain. Thus, the BHE length H is replaced by the rescaled one, $H_r = H/20 = 5.25$ m, and the heat flux Q = 5250 W is replaced by the rescaled one, Q_r = 262.5 W. The thermal conductivities in the vertical direction of all the materials, except the superconductor, are reduced by a rescaling factor $20^2 = 400$. The dimensional quantities characterizing the model and the dimensionless quantities employed in the simulation are reported in Table 2. The rescaled dimensionless total heat flux is given by $Q_r^* = q_l^* \times H_r^* = H_r^* = 70$. The equivalent volumetric heat capacity of the model, $(\rho c)_{eq}$ = 3.054992 MJ/(m³K), is determined by imposing that the heat capacity of the model, per unit length, is equal to that of the BHE, namely 53986.165 J/(mK).

The computational domain is a cylinder with dimensionless vertical length 70 and dimensionless radius 100, equal to that of the circle employed for the 2D simulation of the real BHE. The selected mesh is an unstructured mesh with 83636 triangular elements, and is obtained by a regular refinement of the extremely fine physics-controlled mesh built by the software. Further refinements do not yield relevant changes in the *ftg-function*. A particular of the mesh is illustrated in Figure 4. Values of the *ftg-function* are collected with steps of 0.05 in $\log_{10}(\tau^*)$, in the range $10^{-4} \leq \tau^* \leq 10^2$. The accuracy parameters are the same as in the simulation of the real BHE: relative accuracy 0.0001 and absolute accuracy 0.0001.

In Figure 5, the *ftg-function* obtained by the cylindrical model is compared with that obtained by the 2D simulation of the real BHE. The dimensionless time is reported in logarithmic scale, in the range $-4 \leq \log_{10}(\tau^*) \leq 2$. The figure shows that the model is very accurate, and becomes extremely accurate for $\log_{10}(\tau^*) > 0$. The root-mean-square deviation between the *ftg-function* obtained by the cylindrical model and that obtained by the 2D model of the real BHE is 0.0013 in the whole time interval considered and 0.00013 in the range $0 \leq \log_{10}(\tau^*) \leq 2$.

Table 2. Dimensional quantities that characterize the cylindrical model and corresponding dimensionless quantities employed in the 2D axisymmetric simulation.

| Quantity	Dimensional quantities			Dimensionless quantities	
	Symbol	Unit	Value	Symbol	Value
Model radius	r_b	m	0.075	$r_b{}^*$	1
Superconductor radius	r_{eq}	m	0.0216	$r_{eq}{}^*$	0.288
Rescaled model length	H_r	m	5.25	$H_r{}^*$	70
Rescaled total heat flux	Q_r	W	262.5	$Q_r{}^*$	70
Superconductor thermal conductivity	k_{sc}	W/(mK)	1.8×10^9	$k_{sc}{}^*$	10^9
Annulus thermal conductivity, radial	k_{eq}	W/(mK)	1.86715	$k_{eq}{}^*$	1.037308
Annulus thermal conduct., vertical	k_{eqr}	W/(mK)	0.0046679	$k_{eqr}{}^*$	0.0025933
Ground thermal conductivity, radial	k_g	W/(mK)	1.8	$k_g{}^*$	1
Ground thermal conduct., vertical	k_{gr}	W/(mK)	0.0045	$k_{gr}{}^*$	0.0025
Model volumetric heat capacity	$(\rho c)_{eq}$	MJ/(m³K)	3.054992	$(\rho c)_{eq}{}^*$	1.0183307
Ground volumetric heat capacity	$(\rho c)_g$	MJ/(m³K)	3	$(\rho c)_g{}^*$	1
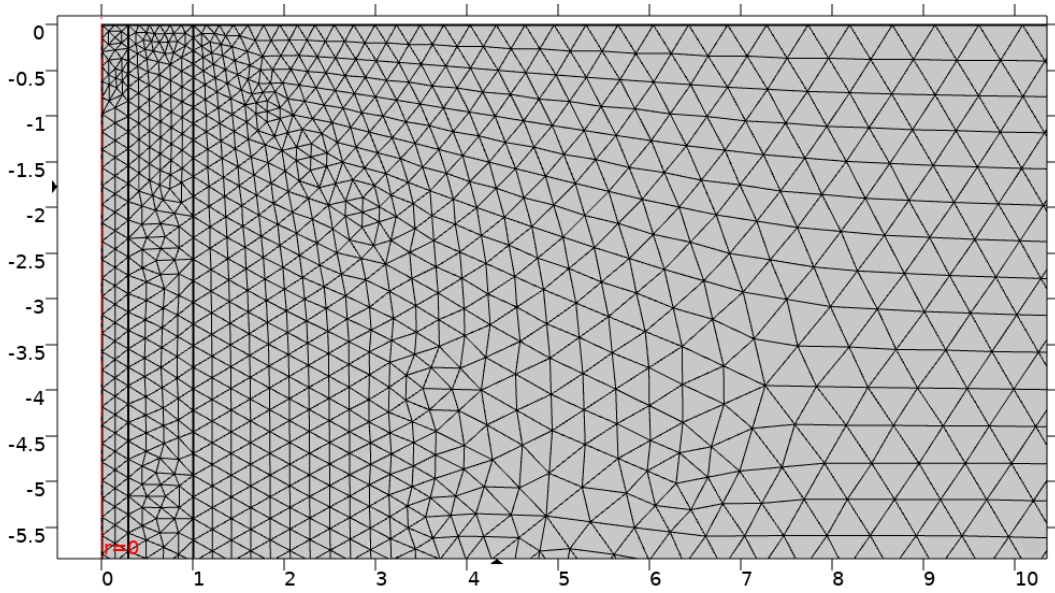
Figure 4. Particular of the mesh employed in the 2D axisymmetric simulation of the cylindrical model with purely radial heat flux.
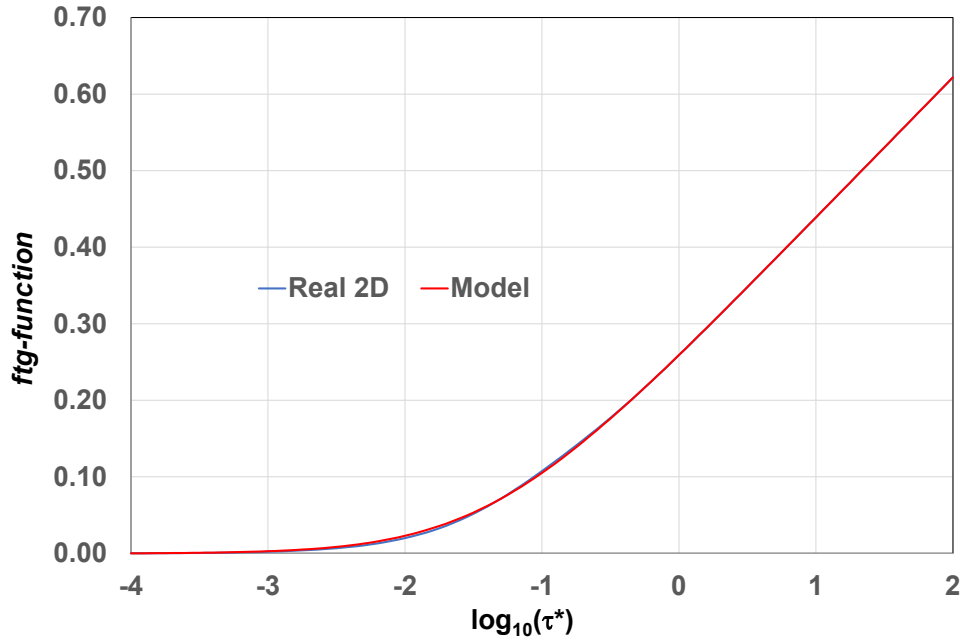
Figure 5. Comparison between the *ftg-function* obtained by the 2D axisymmetric simulation of the model, with purely radial heat flux, and that obtained by the 2D simulation of the real BHE.

3.2. Validation of the 2D axisymmetric simulation code of the cylindrical model

The excellent agreement between the *ftg-function* obtained by the 2D axisymmetric simulation of the cylindrical model and that obtained by the 2D simulation of the real BHE could already be considered as a validation of both the simulation codes. However, a further validation of the simulation code of the model, by comparison with an analytical solution, is presented here.

The semi-analytical BHE model proposed by Man et al. [27] is selected for the validation. In this model, the BHE is represented by a solid cylinder with the same thermal properties as the ground, containing a heat generating cylindrical surface located at $r = r_{eq}$, that represents the fluid. The authors provide two analytical solutions for the model: a 1D solution for the case of purely radial heat flow, and a 2D axisymmetric solution for the case of finite BHE length and uniform heat generation. The 1D solution is considered for the validation, because the 2D axisymmetric case of interest in this paper is not that with uniform heat flux, but that with uniform fluid temperature. In the 1D solution of Ref. [27], the difference between the fluid temperature and the undisturbed ground temperature is given by

$$\theta = -\frac{q_l}{4\pi^2 k_g} \int_0^\pi \text{Ei}\left\{\frac{r_{eq}^2\left[\cos(\phi)-1\right]}{2\tau k_g / (\rho c)_g}\right\} d\phi \ , \tag{22}$$

where q_l is the heat flux per unit length released by the generating surface, ϕ is an angular integration variable, and Ei is the exponential integral function. Equation (22) can be easily written in the dimensionless form

$$ftg\text{-}function = -\frac{1}{4\pi^2}\int_0^\pi \mathrm{Ei}\left\{\frac{r_{eq}^{*2}\left[\cos(\phi)-1\right]}{2\tau^*}\right\}d\phi \ . \tag{23}$$

The *ftg-function* yielded by Eq. (23) with $r_{eq}{}^* = 0.288$ is determined by a numerical integration, in the dimensionless-time range $-3 \le \log_{10}(\tau^*) \le 6$, with steps of 0.05 in $\log_{10}(\tau^*)$.

The cylindrical model is modified, to reproduce the conditions of the semi-analytical solution. The superconductor is replaced by a material having the same thermal properties as the annulus and the ground, with a rescaled thermal conductivity in the vertical direction, k_{scr}. A heat generating surface that represents the fluid is placed at $r^* = r_{eq}{}^* = 0.288$. Some dimensionless parameters of Table 2 are modified, as follows: $k_{sc}{}^* = 1$, $k_{scr}{}^* = 0.0025$, $k_{eq}{}^* = 1$, $k_{eqr}{}^* = 0.0025$, $(\rho c)_{eq}{}^* = 1$. The surface heat source intensity is set equal to $Q_r{}^*/(2\pi\, r_{eq}{}^* H^*) = 1/(2\pi \times 0.288)$. The computational domain is a cylinder with dimensionless vertical length 70 and dimensionless radius 2500. The mesh is obtained by two regular refinements of the extremely fine physics-controlled mesh built by the software, and has 107360 triangular elements. The relative accuracy and the absolute accuracy are set equal to 0.0001. The results are collected with steps of 0.05 in $\log_{10}(\tau^*)$, in the range $-3 \le \log_{10}(\tau^*) \le 2$. A comparison between the *ftg-function* obtained by Eq. (23) and that obtained by a 2D axisymmetric finite-element simulation of the cylindrical model is illustrated in Figure 6. The figure shows an excellent agreement between the *ftg-function* obtained by the semi-analytical method and that obtained by the finite-element simulation. The root-mean-square deviation is 0.000132, and corresponds to 0.023% of the mean value of the *ftg-function*.
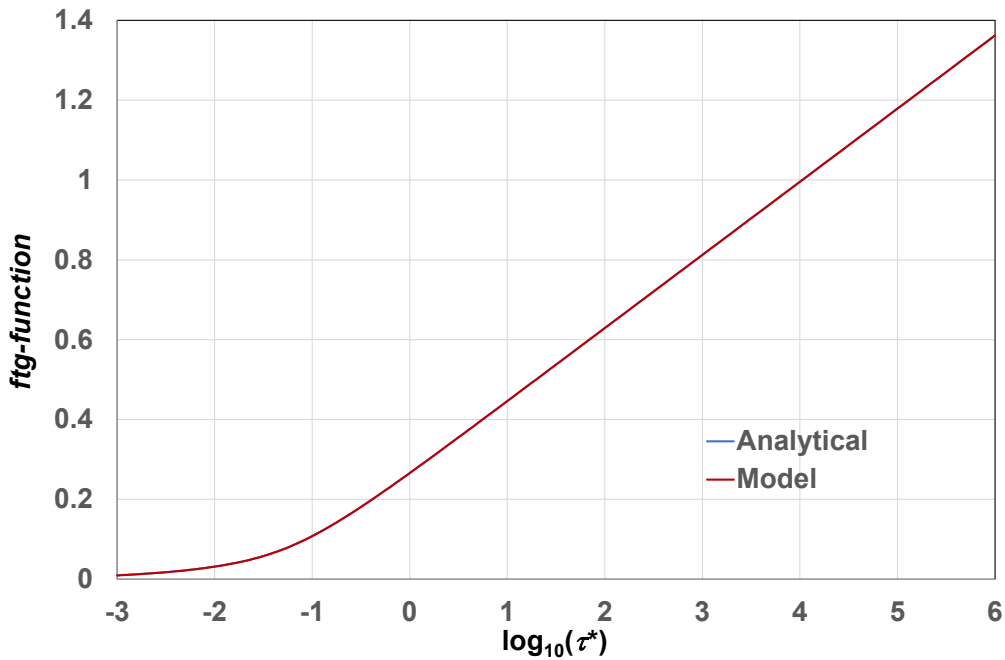

Figure 6. Comparison between the *ftg-function* obtained by the 2D axisymmetric simulation of the cylindrical model, with purely radial heat flux, and that obtained by the analytical solution.

4. Values of the dimensionless parameters

The following dimensionless parameters characterize a single-line bore field, in the cylindrical model: dimensionless BHE thermal resistance, R_b^*; dimensionless radius of the superconductor that represents the fluid, r_{eq}^*; dimensionless volumetric heat capacity of the model, $(\rho c)_{eq}^*$; dimensionless BHE length, H^*; dimensionless distance between adjacent BHEs, d^*; dimensionless buried depth, B_d^*.

The dimensionless buried depth has not an important effect on the *ftg-function*. Therefore, in our study it is fixed, with value $B_d^* = 24$. For $r_b = 0.075$ m, this value corresponds to $B_d = 1.80$ m, that is a common buried depth for temperate climates. The following values of R_b^* are considered: 0.1, 0.2, 0.3. They correspond to $R_b = 0.05$ mK/W, 0.10 mK/W and 0.15 mK/W for $k_g = 2$ W/(mK). The following values are considered for r_{eq}^* and $(\rho c)_{eq}^*$: $r_{eq}^* = 0.20, 0.35, 0.50$; $(\rho c)_{eq}^* = 0.6, 1.1, 1.6$. These values cover all the cases considered in Ref. [30]. For H^*, the values $H^* = 800, 1400, 2000$ are considered. They correspond to $H = 60$ m, 105 m, 150 m, for $r_b = 0.075$ m. Finally, the following values of d^*, for bore fields with two or more BHEs, are considered: $d^* = 60, 90, 120$. These values correspond to $d = 4.50$ m, 6.75 m and 9.00 m, for $r_b = 0.075$ m.

The *ftg-functions* for bore fields in a single line with isothermal fluid are calculated in the dimensionless-time range $10^{-4} \leq \tau^* \leq 10^6$. For a ground thermal diffusivity equal to 7.5×10^{-7} m²/s and $r_b = 7.5$ cm, this range corresponds to the time interval 0.75 s $\leq \tau \leq 7.5 \times 10^9$ s ≈ 237.8 years. The results for $10^{-4} \leq \tau^* \leq 10^{-2}$ should be considered mainly as benchmark values for simulations performed under the assumption of isothermal fluid and may be not quite accurate for real BHEs.

5. Short-term and long-term *ftg-functions*

With a fixed value of B_d^*, five dimensionless parameters are necessary to identify the model of a bore field with two or more BHEs, namely $R_b^*, r_{eq}^*, (\rho c)_{eq}^*, H^*, d^*$. With three values for each parameter, $3^5 = 243$ combinations of parameters would be necessary to provide a suitable data base of *ftg-functions*, for each bore field. However, preliminary simulations revealed that not all the dimensionless parameters have significant effects on the *ftg-function* during the whole dimensionless-time interval $10^{-4} \leq \tau^* \leq 10^6$. It is possible to find a value of the dimensionless time, τ_0^*, such that: for $\tau^* \leq \tau_0^*$ the *ftg-function* depends only on R_b^*, r_{eq}^*, and $(\rho c)_{eq}^*$; for $\tau^* \geq \tau_0^*$ the *ftg-function* depends only on R_b^*, H^*, d^*. Therefore, the simulation results are divided in two groups: simulation results for $\tau^* \leq \tau_0^*$, that yield short-term *ftg-functions*; simulation results for $\tau^* \geq \tau_0^*$, that yield long-term *ftg-functions*. The short-term *ftg-functions* are computed for a single BHE, with $H^* = 1400$. In fact, the interference between BHEs has no appreciable effects for $\tau^* \leq \tau_0^*$. Thus, 3^3 short-term *ftg-functions* are obtained, by combinations of $R_b^*, r_{eq}^*, (\rho c)_{eq}^*$. For each value of R_b^*, the short-term *ftg-functions*

are slightly modified, in a narrow neighborhood of $\tau_0{}^*$, so that at $\tau_0{}^*$ they have all the same value as the *ftg-function* for $r_{eq}{}^* = 0.35$ and $(\rho c)_{eq}{}^* = 1.1$. The long-term *ftg-functions* are computed for each bore field. Thus, 3^3 long-term *ftg-functions* are obtained for each bore field with at least 2 BHEs, by combinations of $R_b{}^*$, H^*, d^*, and 3^2 long term *ftg-functions* for the single BHE, where d^* is not a parameter. The long-term *ftg-functions* are computed with $r_{eq}{}^* = 0.35$ and $(\rho c)_{eq}{}^* = 1.1$. For each value of $R_b{}^*$, the long-term *ftg-functions* are slightly modified, in a narrow neighborhood of $\tau_0{}^*$, so that at $\tau_0{}^*$ they coincide with each other and with the short-term *ftg-function* for the same value of $R_b{}^*$. The corrections usually change only the fourth decimal digit or, exceptionally, also the third decimal digit by one unit. By this method, all the *ftg-functions* are perfectly joined at $\tau_0{}^*$. The value $\tau_0{}^* = 10^2$ is selected, that corresponds to $\tau = 7.5 \times 10^5$ s ≈ 208.33 h for a ground thermal diffusivity equal to 7.5×10^{-7} m^2/s and $r_b = 7.5$ cm.

Since $\tau_0{}^*$ is much shorter than the dimensionless time required to have appreciable effects of interference between BHEs, the independence of the short-term *ftg-functions* from H^* will be proved with reference to a single BHE. Similarly, since the effects of $r_{eq}{}^*$ and $(\rho c)_{eq}{}^*$ on the *ftg-function* vanish before the interference between BHEs takes place, the independence of the long-term *ftg-functions* from $r_{eq}{}^*$ and $(\rho c)_{eq}{}^*$ will be proved for one BHE.

5.1. Independence of the short-term *ftg-functions* from H^*

In order to prove that the *ftg-functions* are independent of H^* for $\tau^* \leq 10^2$, the results of computations performed with $R_b{}^* = 0.2$, $r_{eq}{}^* = 0.35$, $(\rho c)_{eq}{}^* = 1.1$, and $H^* = 800, 1400, 2000$ are presented. Similar results hold for other combinations of $R_b{}^*$, $r_{eq}{}^*$, and $(\rho c)_{eq}{}^*$.

2D axisymmetric simulations of the cylindrical model are performed, that differ only in the dimensionless BHE length and, as a consequence, on the total dimensionless height of the computational domain. The whole interval of dimensionless time $10^{-4} \leq \tau^* \leq 10^6$ is considered. $B_d{}^* = 24$ is assumed, and a rescaling ratio 20 in the vertical direction is employed. So, one has $B_{dr}{}^* = 1.2$ and $H_r{}^* = 40, 70, 100$. The top of the BHE is placed at $z_r{}^* = 0$. The computational domain is a cylinder with vertical extension from $z_r{}^* = 1.2$ to $z_r{}^* = -(H_r{}^* + 125)$, and dimensionless radius 2500. The initial condition is $T^* = 0$, in the whole computational domain. The boundary condition at the ground surface is $T^* = 0$, while the vertical and bottom boundaries of the computational domain are assumed to be adiabatic. The size of the domain is such that if the adiabatic boundary condition at the vertical and bottom boundaries is replaced by $T^* = 0$, no change of the *ftg-functions* occurs within the digits of interest. The rescaled total heat flux is $Q_r{}^* = H_r{}^*$. The dimensionless thermal conductivity of the superconductor, that of the ground in the radial direction and that of the ground in the vertical direction are the same as in Table 2, namely $k_{sc}{}^* = 10^9$, $k_g{}^* = 1$ and $k_{gr}{}^* = 0.0025$. The

dimensionless thermal conductivity of the cylindrical annulus in the radial direction is that corresponding to $R_b{}^* = 0.2$, namely $k_{eq}{}^* = 0.835422$, and the rescaled one, in the vertical direction, is $k_{eqr}{}^* = 0.00208855$. The relative accuracy and the absolute accuracy are both equal to 0.0001. Values of the *ftg-functions* are collected with steps of 0.05 in $\log_{10}(\tau^*)$. In each case, the selected mesh is the extremely fine physics-controlled mesh built by the software, with two regular refinements. The number of triangular elements is 103904, 143904, 186432, respectively for $H_r{}^* = 40, 70, 100$. A particular of the mesh, for $H_r{}^* = 70$, is illustrated in Figure 7. The particular, focused on the upper part of the BHE, shows that the thin ground cylinder above the superconductor has been removed, in order to impose the heat flux boundary condition at the upper surface of the superconductor.
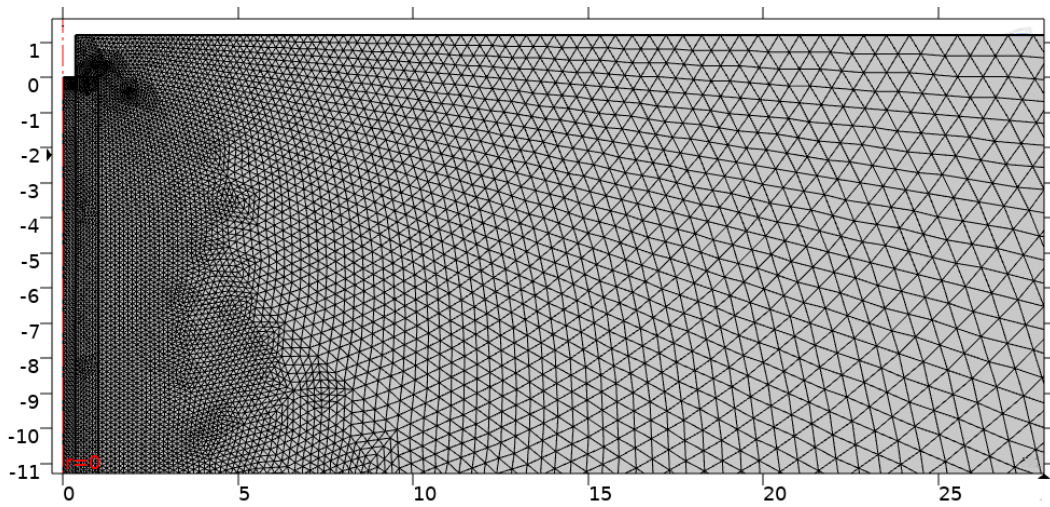
Figure 7. Particular of the mesh employed in the 2D axisymmetric simulation of the model with $R_b{}^*$ = 0.2, $r_{eq}{}^* = 0.35$, $(\rho c)_{eq}{}^* = 1.1$, $H^* = 1400$.

The mesh independence of the *ftg-function*, for $H_r{}^* = 70$, is illustrated in Figure 8. The figure compares the *ftg-functions* obtained with different meshes: Mesh 1, having 8994 triangular elements; Mesh 2, obtained by a regular refinement of Mesh 1 and having 35976 triangular elements; Mesh 3, obtained by a regular refinement of Mesh 2 and having 143904 triangular elements. The comparison shows that the *g-functions* are graphically indistinguishable when plotted in the whole range of dimensionless time, $10^{-4} \leq \tau^* \leq 10^6$.

A particular of Figure 8, in the range $10^5 \leq \tau^* \leq 10^6$, is reported in Figure 9. It shows that the differences between the results obtained by Mesh 3 and those obtained by Mesh 2 are much lower than the differences between the results obtained by Mesh 2 and those obtained by Mesh 1. The maximum difference is 0.0007. A further refinement would yield a much lower maximum difference from the results of Mesh 3. Therefore, the *ftg-function* obtained by Mesh 3 can be considered as mesh independent for the scope of the present paper. Mesh 3 or similar meshes are employed hereafter in all the simulations of a single BHE.
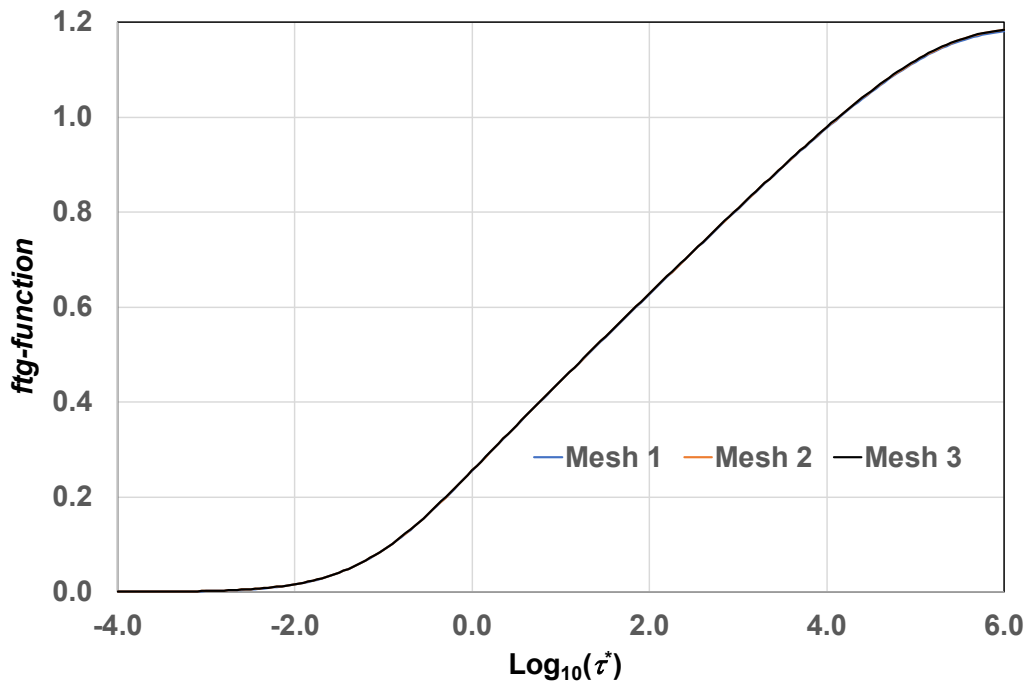
Figure 8. Proof of mesh-independence of the simulation results of the model obtained with Mesh 3 (selected mesh), for $R_b^* = 0.2$, $r_{eq}^* = 0.35$, $(\rho c)_{eq}^* = 1.1$, $H^* = 1400$.
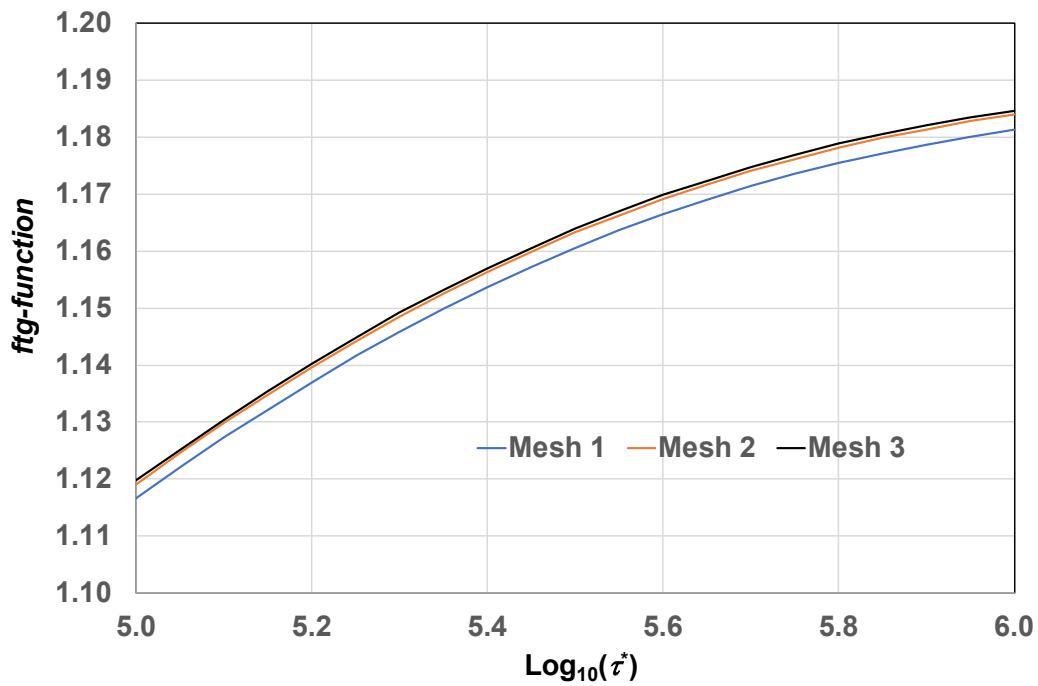

Figure 9. Particular of Figure 8, in the range $10^5 \leq \tau^* \leq 10^6$.

The independence of the results from the domain extension is checked by replacing the adiabatic condition at the vertical and bottom boundaries with the isothermal condition $T^* = 0$. The first condition overestimates the temperature changes with respect to the real situation of infinite ground, the second underestimates them. The maximum difference between the *ftg-functions* obtained with these conditions is 0.0001. Moreover, the independence of the results from the dimensionless thermal

conductivity of the superconductor is checked, by replacing $k_s^* = 10^9$ with $k_s^* = 10^{10}$. Again, the highest discrepancy is 0.0001.

The independence of the short-term *ftg-functions* from H^* is illustrated in Figure 10, where diagrams of the *ftg-functions* with $H^* = 800$, 1400 and 2000 are compared graphically, for $R_b^* = 0.2$, $r_{eq}^* = 0.35$, $(\rho c)_{eq}^* = 1.1$. The figure shows that the effects of H^* on the *ftg-functions* are negligible up to $\tau^* = 10^2$. For $\tau^* = 10^2$, the difference between the *ftg-function* for $H^* = 1400$ and that for $H^* = 800$ is 0.0013, and the difference between the *ftg-function* for $H^* = 2000$ and that for $H^* = 1400$ is 0.0005. Therefore, the highest possible error due to neglecting the effect of H^* on the short-term *ftg-functions*, that are computed with $H^* = 1400$, is 0.0013.

5.2. Independence of the long-term *ftg-functions* from r_{eq}^* and $(\rho c)_{eq}^*$.

In order to prove that the *ftg-functions* are independent of r_{eq}^* for $\tau^* \geq 10^2$, the *ftg-functions* of a single BHE for $R_b^* = 0.2$, $H^* = 1400$, $(\rho c)_{eq}^* = 1.1$, are analyzed with three different values of r_{eq}^*, namely 0.20, 0.35, 0.50. The corresponding values of the dimensionless thermal conductivity of the cylindrical annulus in the radial direction are $k_{eq}^* = 1.28075$, 0.835422, 0.551589, and the rescaled values, along z, are $k_{eqr}^* = 0.00320187$, 0.00208855, 0.00137897. The meshes employed are the extremely fine physics-controlled meshes built by the software, with two regular refinements, and have 208608, 143904, 117168 triangular elements, respectively. The relative accuracy and the absolute accuracy are again equal to 0.0001.
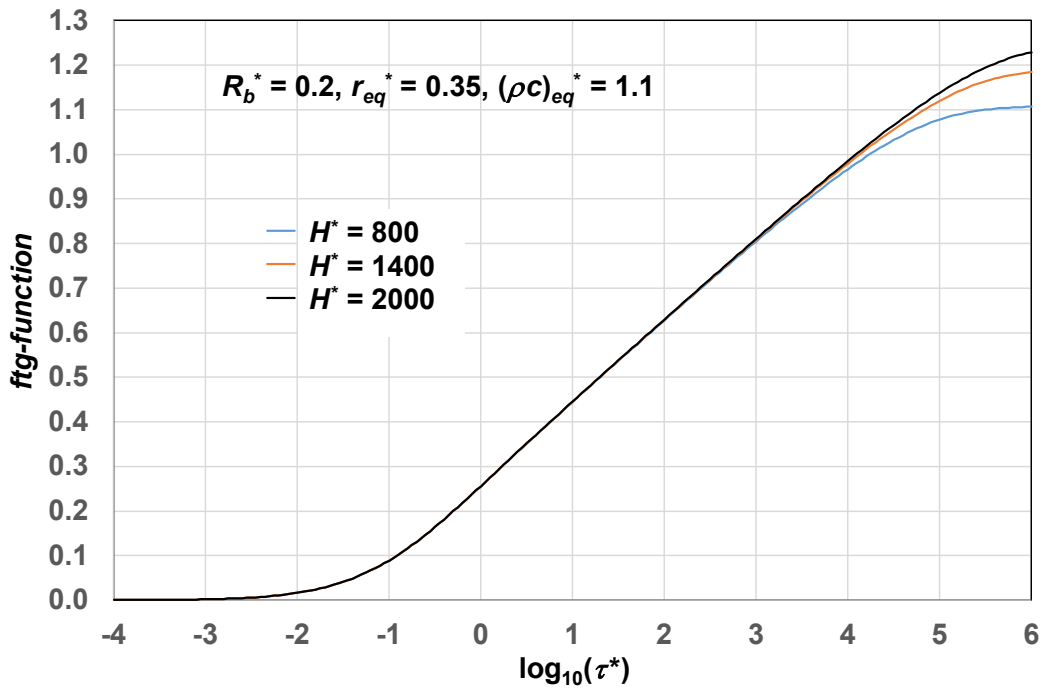

Figure 10. Proof of independence of the short-term *ftg-functions* from H^*, for $R_b^* = 0.2$, $r_{eq}^* = 0.35$, $(\rho c)_{eq}^* = 1.1$.

The *ftg-functions* for $R_b{}^* = 0.2$, $H^* = 1400$, $(\rho c)_{eq}{}^* = 1.1$, and $r_{eq}{}^* = 0.20, 0.35, 0.50$ are compared in Figure 11. The figure shows that the effect of $r_{eq}{}^*$ on the *ftg-function* is negligible for $\tau^* \geq 10^2$. For $\tau^* = 10^2$, the difference between the *ftg-function* for $r_{eq}{}^* = 0.20$, and that for $r_{eq}{}^* = 0.35$ is 0.0003, and the difference between the *ftg-function* for $r_{eq}{}^* = 0.35$ and that for $r_{eq}{}^* = 0.50$ is 0.0004. Therefore, the highest possible error due to neglecting the effect of $r_{eq}{}^*$ on the long-term *ftg-functions*, that are computed with $r_{eq}{}^* = 0.35$, is 0.0004.

In order to prove that the *ftg-functions* are independent of $(\rho c)_{eq}{}^*$ for $\tau^* \geq 10^2$, in Figure 12 diagrams of the *ftg-functions* for $R_b{}^* = 0.2$, $H^* = 1400$, $r_{eq}{}^* = 0.35$, are reported with three different values of $(\rho c)_{eq}{}^*$, namely 0.6, 1.1, 1.6. The input parameters, the mesh and the accuracy parameters are the same as for the case $R_b{}^* = 0.2$, $H^* = 1400$, $r_{eq}{}^* = 0.35$, $(\rho c)_{eq}{}^* = 1.1$, already illustrated in Figure 11, except for the values of $(\rho c)_{eq}{}^*$. The figure show that the effect of $(\rho c)_{eq}{}^*$ can be considered as negligible for $\tau^* \geq 10^2$. For $\tau^* = 10^2$, the difference between the *ftg-function* for $(\rho c)_{eq}{}^* = 0.6$ and that for $(\rho c)_{eq}{}^* = 1.1$ is 0.0013, and the difference between the *ftg-function* for $(\rho c)_{eq}{}^* = 1.1$ and that for $(\rho c)_{eq}{}^* = 1.6$ is 0.0013. Therefore, the highest possible error due to neglecting the effect of $(\rho c)_{eq}{}^*$ on the long-term *ftg-functions*, that are computed with $(\rho c)_{eq}{}^* = 1.1$, is 0.0013.
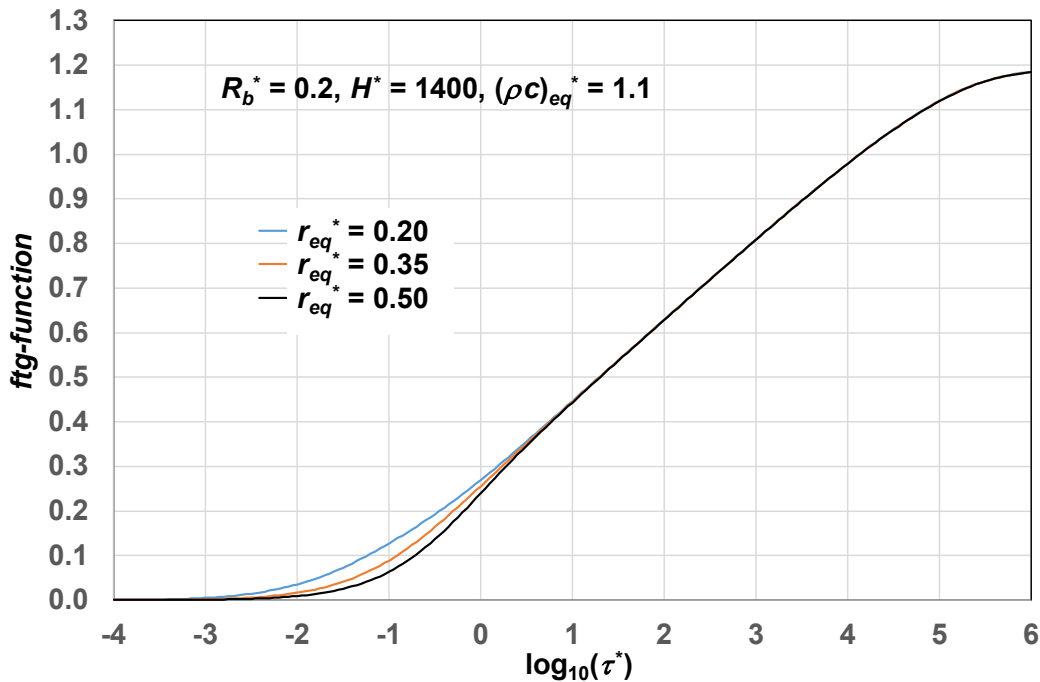

Figure 11. Proof of independence of the long-term *ftg-functions* from $r_{eq}{}^*$, for $R_b{}^* = 0.2$, $H^* = 1400$, $(\rho c)_{eq}{}^* = 1.1$.
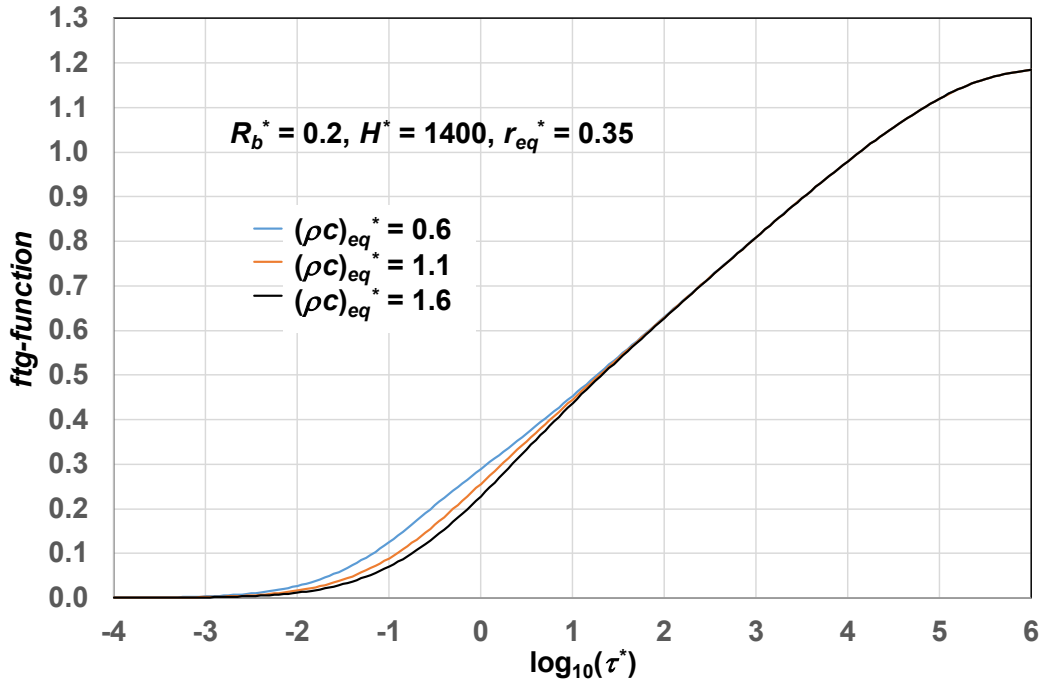
Figure 12. Proof of independence of the long-term *ftg-functions* from $(\rho c)_{eq}{}^*$, for $R_b{}^* = 0.2$, $H^* = 1400$, $r_{eq}{}^* = 0.35$.

6. Short-term *ftg-functions* for BHEs with isothermal fluid

The short-term *ftg-functions* have been computed for a single BHE, with $H^* = 1400$, but they are valid also for BHE fields with several BHEs and for different values of H^*. Due to the slight corrections, they have the same value at $\tau_0{}^* = 10^2$, for each value of $R_b{}^*$.
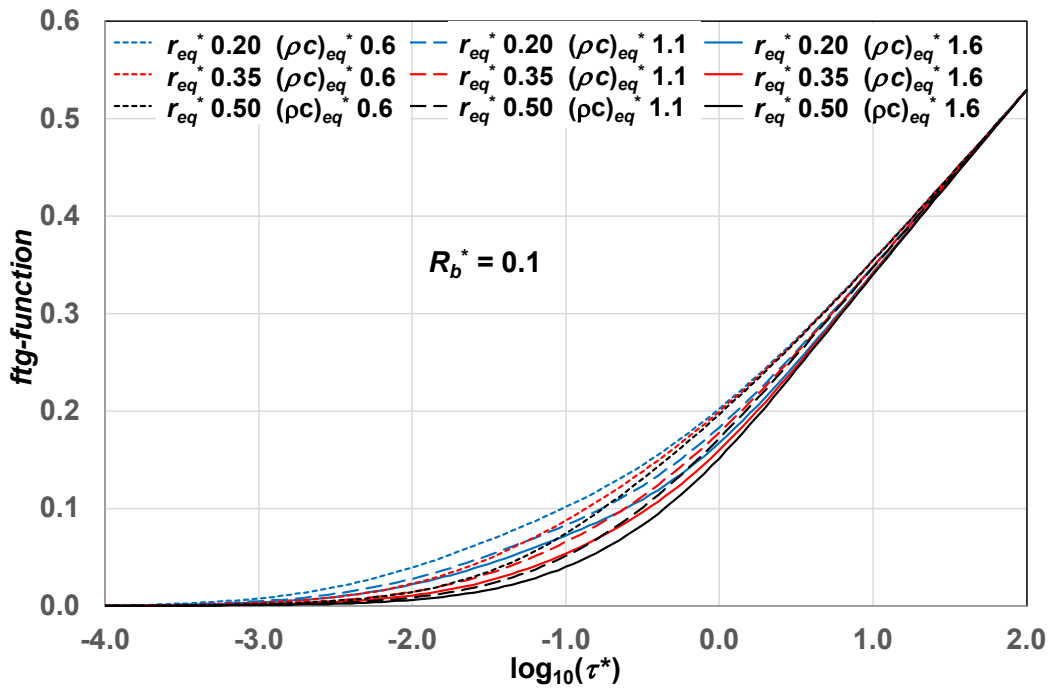

Figure 13. Short-term *ftg-functions* for $R_b{}^* = 0.1$.
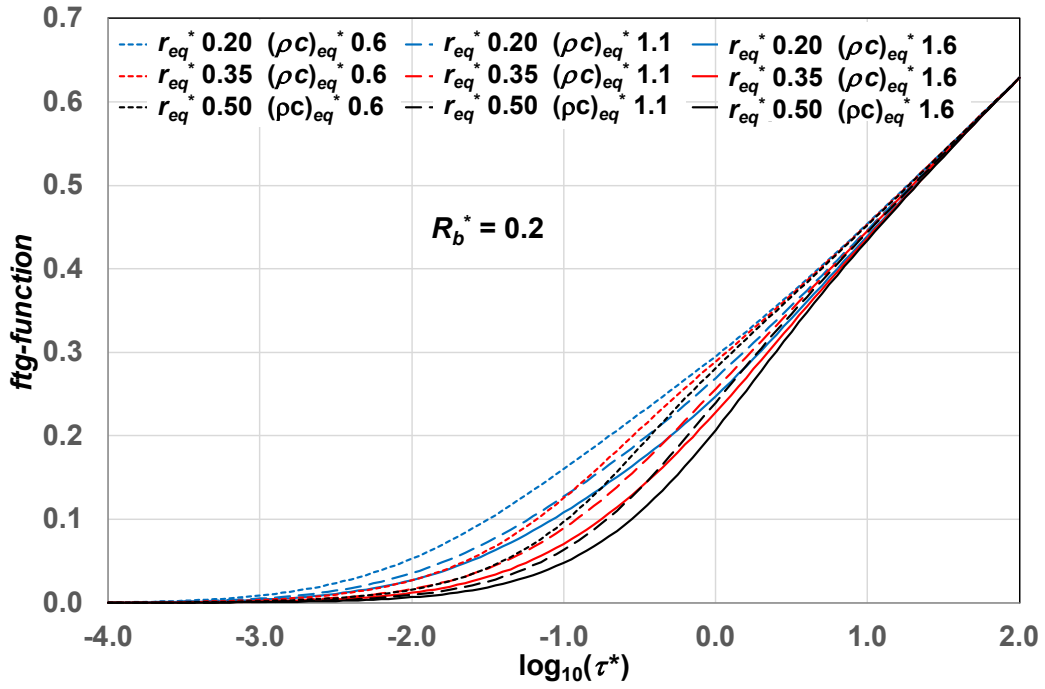
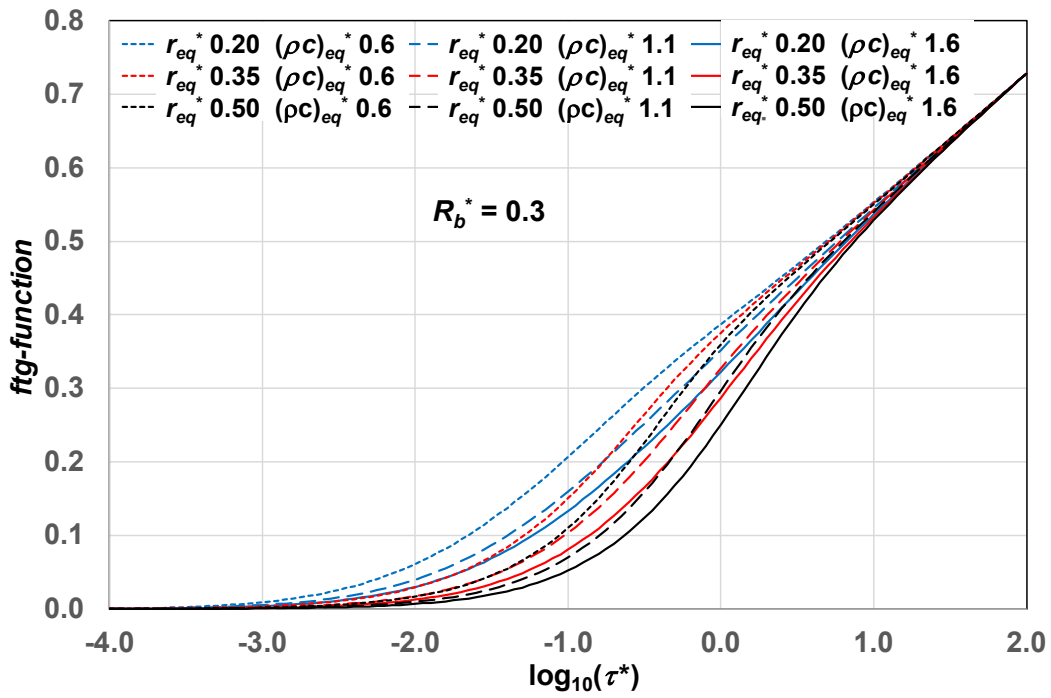Figure 14. Short-term *ftg-functions* for $R_b^* = 0.2$.

Figure 15. Short-term *ftg-functions* for $R_b^* = 0.3$.

The short-term *ftg-functions* for $R_b^* = 0.1$, 0.2 and 0.3 are illustrated in Figures 13, 14 and 15, respectively. The figures show that the short-term *ftg-functions* are increasing functions of R_b^* and decreasing functions of r_{eq}^* and of $(\rho c)_{eq}^*$. The dependence on r_{eq}^* and of $(\rho c)_{eq}^*$ is stronger for higher values of R_b^*.

Tables of the short-term *ftg-functions* of BHEs with isothermal fluid, with steps of 0.05 in $\log_{10}(\tau^*)$, are reported in the Excel file "Short-term *ftg-functions*", available in the Repository AMSActa (see Data Availability Section).

7. Long-term *ftg-functions* for a single BHE with isothermal fluid

The long-term *ftg-functions* for a single BHE with isothermal fluid are illustrated in Figure 16. The figure shows that, as expected, they are increasing functions of both R_b^* and H^*. A table of the long-term *ftg-functions* for a single BHE, with steps of 0.05 in $\log_{10}(\tau^*)$, is reported in the Excel file "Long-term *ftg-functions* for a single BHE", available in the Repository AMSActa (see Data Availability Section).
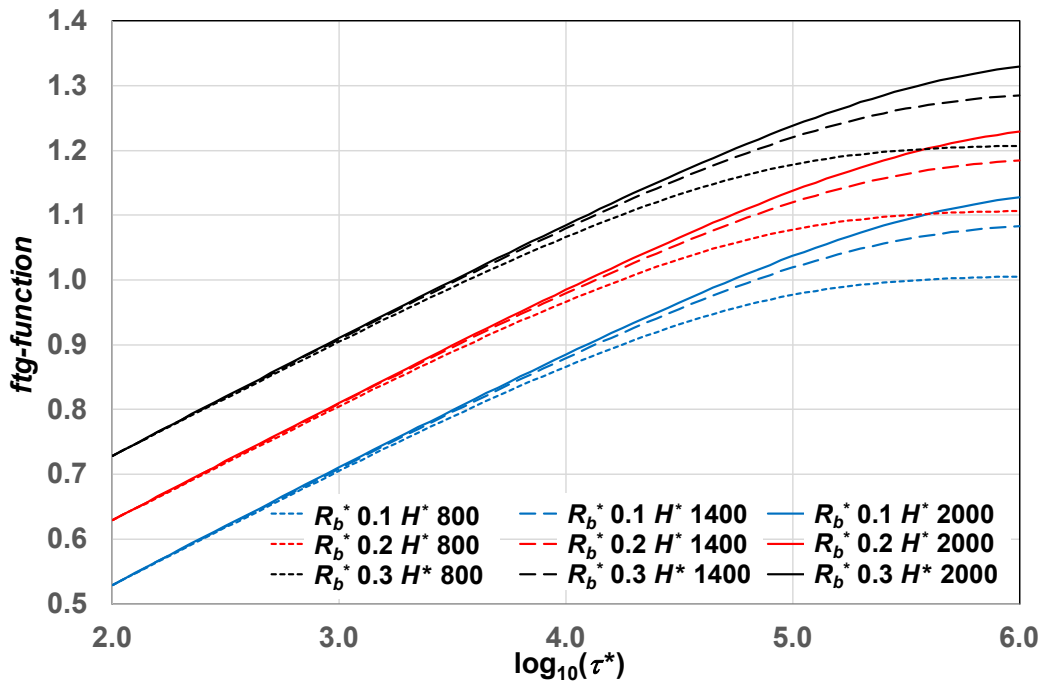

Figure 16. Long-term *ftg-functions* for a single BHE with isothermal fluid.

8. Long-term *ftg-functions* for a line of 2 BHEs with isothermal fluid

The long-term *ftg-functions* for a line of 2 BHEs with isothermal fluid have been determined by 3D finite-element simulations, with the following values of the dimensionless parameters: $B_d^* = 24$; $R_b^* = 0.1, 0.2, 0.3$; $H^* = 800, 1400, 2000$; $d^* = 60, 90, 120$. For each geometric configuration, a computational domain with a symmetry plane placed between the BHEs, at an equal distance from each of them, has been employed. In this domain, the ground is a rectangular parallelepiped with dimensionless horizontal sides equal to $2500 + d^*/2$ along the direction, x, that connects the axes of the BHEs, equal to 5000 along y, and equal to $(B_d^* + H^* + 2500)/20$ along z, where 20 is the rescaling coefficient adopted in the vertical direction. Each BHE is modeled as in the previous sections.

In order to obtain equal fluid temperatures in the BHEs, the vertical superconductive cylinders representing the fluid are connected with a horizontal superconductive bar placed above the ground. The bar has a square cross section with dimensionless sides equal to 2, and is connected with each cylinder representing the fluid by means of additional superconductive material: a vertical cylinder, with the same diameter as the sides of the bar, and a vertical cone that reduces the diameter of the cylinder to that of the fluid. The dimensionless thermal properties of the superconductive material are $k_s^* = 10^9$ and $(\rho c)_{sc}^* = 0.01$. A particular of the computational domain, with the mesh adopted in the final computations, denoted by Mesh 2, is illustrated in Figure 17. The figure refers to the geometry with $H^* = 1400$ and $d^* = 90$, where the employed mesh consists of 6 079 360 tetrahedral elements. The part of the figure in black and gray represents the superconductive material that interconnects the BHEs and, in transparency, the superconductive material that represents water, while the part in blue and light blue represents the other elements of the computational domain.
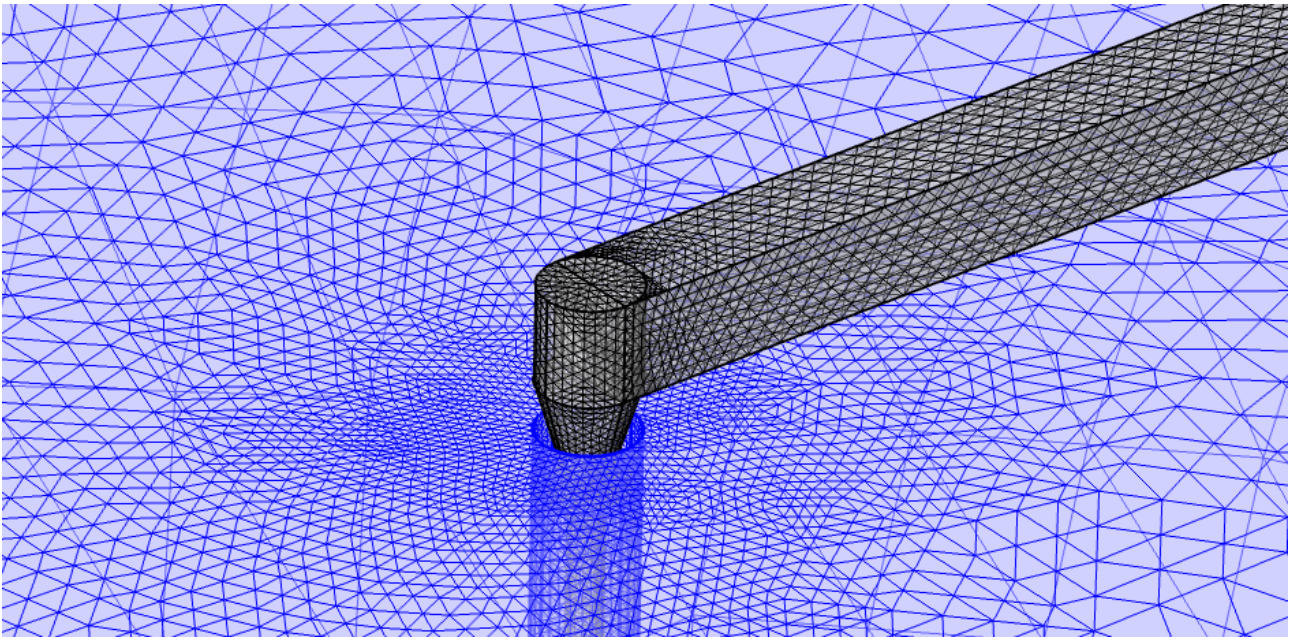

Figure 17. Particular of the computational domain and mesh employed for the final simulation of the field with 2 BHEs, $H^* = 1400$, $d^* = 90$, $R_b^* = 0.2$.

Before performing the final computations for the lines of 2 BHEs, the accuracy of the 3D simulation code has been checked by comparing the results yielded by this code with those obtained by the 2D axisymmetric code employed for the simulations of the single BHEs. For this purpose, with reference to the field with $H^* = 1400$, $d^* = 90$ and $R_b^* = 0.2$, the distance between the BHEs has been increased from $d^* = 90$ to $d^* = 5000$, to reach the thermal independence of the BHEs. The half-length of the superconductive horizontal bar, from the axis of the left BHE, has been kept equal to 45, and an adiabatic boundary has been placed at the right end of the bar.

Two meshes have been employed to check the accuracy of the 3D simulations: Mesh 1, with 936 912 tetrahedral elements, obtained by a regular refinement of the extremely fine physics-controlled mesh built by the software; Mesh 2, with 7 495 296 tetrahedral elements, obtained by a second regular refinement. In Figure 18, the long-term *ftg-functions* obtained by Mesh 1 and by Mesh 2 are compared with that obtained by the 2D axisymmetric code, in the long-term range $2 \leq \log_{10}(\tau^*) \leq 6$. A particular, in the range $5 \leq \log_{10}(\tau^*) \leq 6$, is reported in Figure 19, and illustrates better the convergence of Mesh 2 to the 2D axisymmetric *ftg-function*. The root-mean-square deviation between the long-term *ftg-function* obtained by the 3D simulation with Mesh 2 and that obtained by the 2D axisymmetric simulation is 0.0005, and corresponds to 0.054% of the mean value of the long-term *ftg-function*. This result shows the high accuracy reached by the 3D simulation performed with Mesh 2.

The final simulations to determine the long-term *ftg-functions* for a line of 2 BHEs with isothermal fluid have been performed by meshes, denoted by Mesh 2, obtained by two regular refinements of the extremely fine physics-controlled mesh built by the software. The number of tetrahedral elements ranged from 3 937 408, for $H^* = 800$ and $d^* = 60$, to 8 332 800, for $H^* = 2000$ and $d^* = 120$.

The effects of the dimensionless BHE length on the long-term *ftg-function*, for $R_b{}^* = 0.2$ and $d^* = 90$, are illustrated in Figure 20. The figure shows that, as expected, higher values of H^* yield higher values of the *ftg-function* in the long term, due to the lower beneficial effect of the constant temperature at the ground surface. The difference between the *ftg-functions* with $H^* = 1400$ and $H^* = 800$ is more relevant that that between the *ftg-functions* with $H^* = 2000$ and $H^* = 1400$.
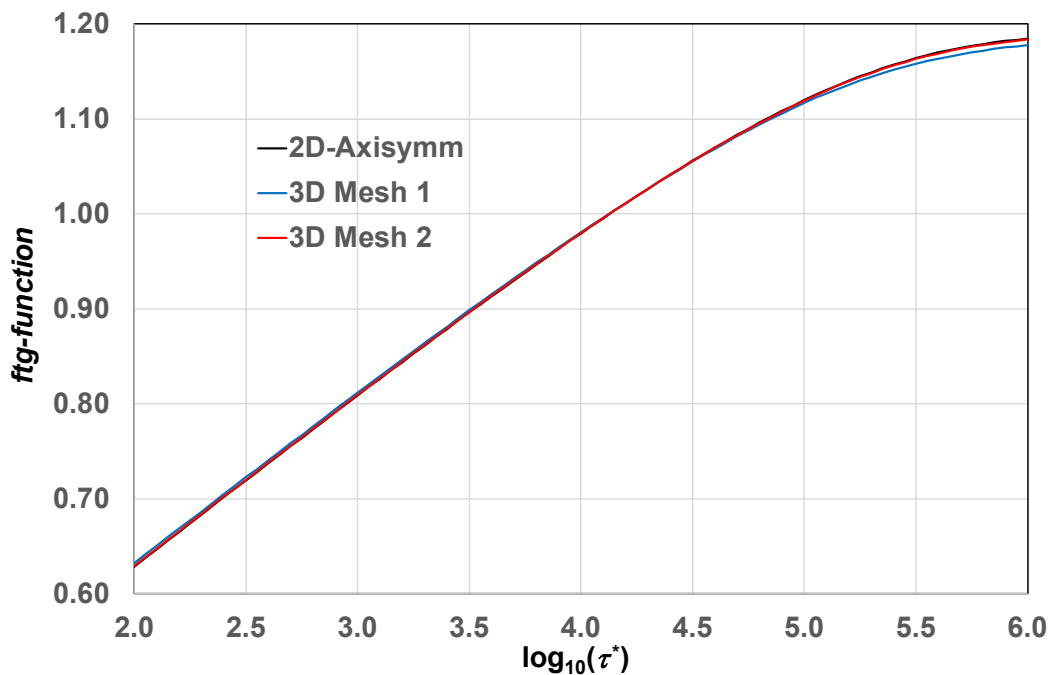

Figure 18. Comparison between the long-term *ftg-functions* obtained by 3D simulations with Mesh 1 and with Mesh 2 and that obtained by the 2D axisymmetric code, for a single BHE with $H^* = 1400$ and $R_b{}^* = 0.2$
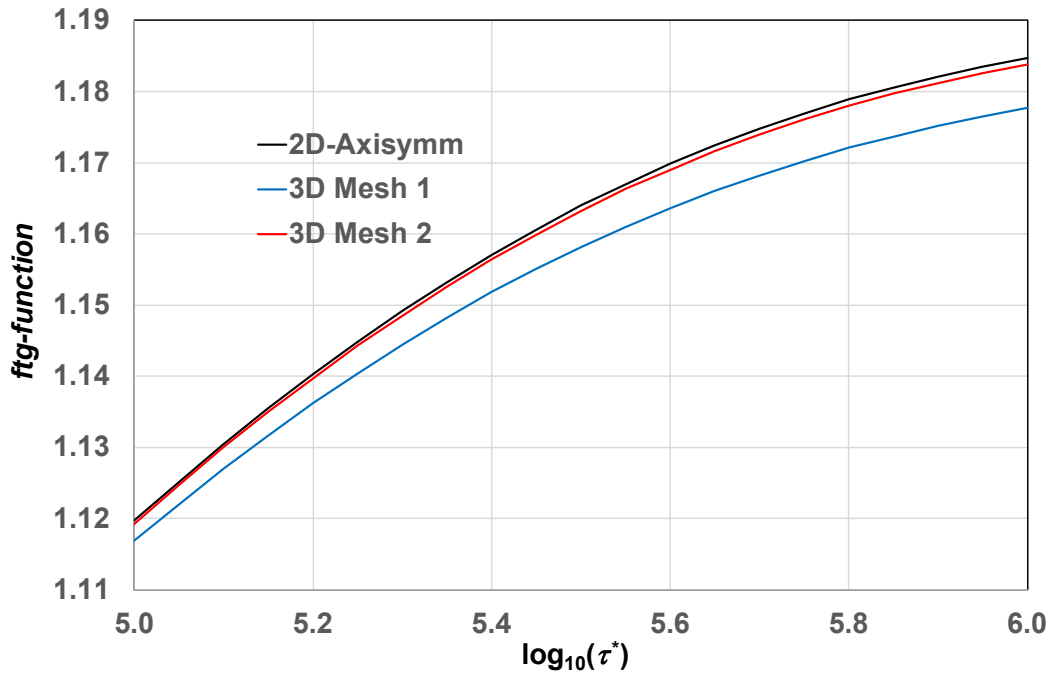
Figure 19. Particular of Figure 18, in the range $10^5 \leq \tau^* \leq 10^6$.

The effects of d^* on the *ftg-function*, for $R_b^* = 0.2$ and $H^* = 1400$, are illustrated in Figure 21. As expected, the *ftg-function* is higher for lower values of d^*, due to the higher thermal interference between the BHEs, and the difference between the *ftg-functions* for $d^* = 60$ and $d^* = 90$ is higher than that between the *ftg-functions* for $d^* = 90$ and $d^* = 120$.
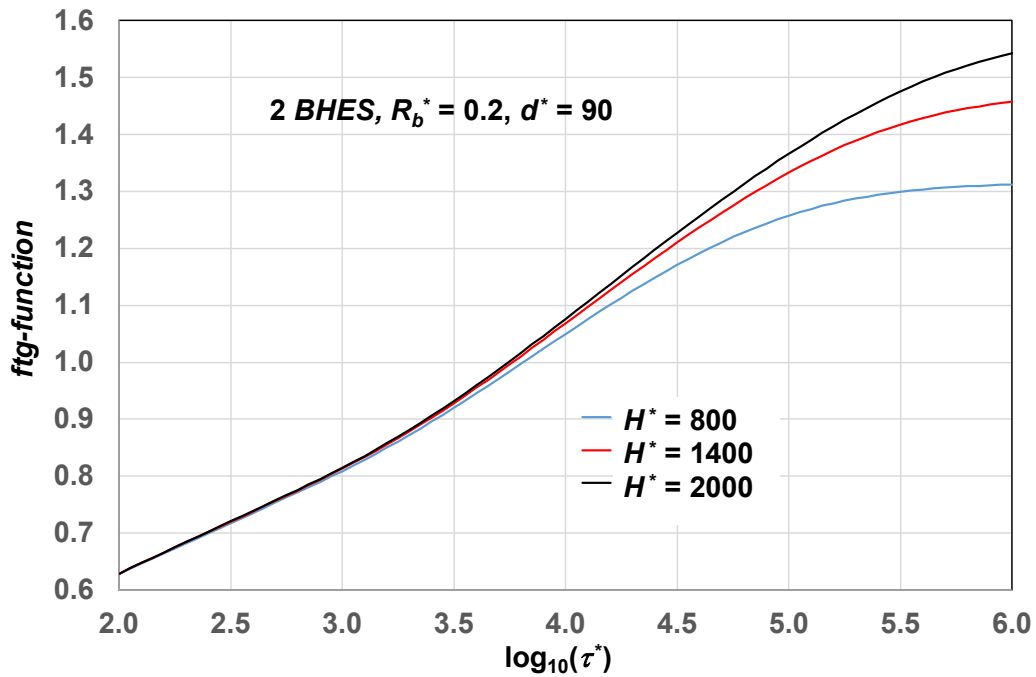

Figure 20. Effects of H^* on the long-term *ftg-function* of a field with 2 BHEs, for $R_b^* = 0.2$ and $d^* = 90$.
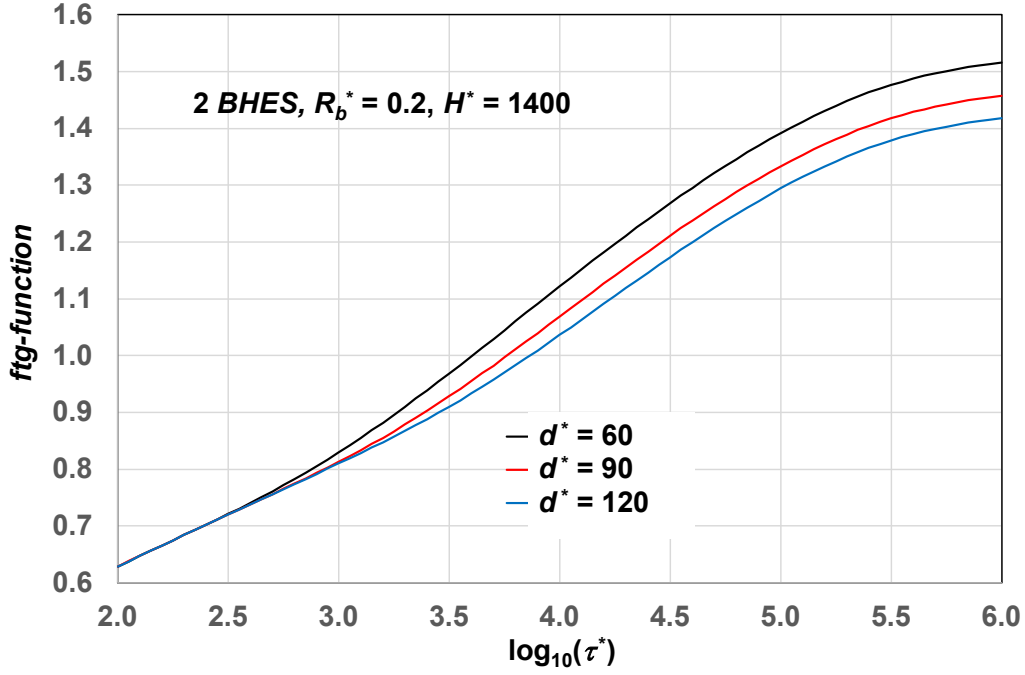
Figure 21. Effects of d^* on the long-term *ftg-function* of a field with 2 BHEs, for $R_b^* = 0.2$ and $H^* = 1400$.

The effects of R_b^* on the long-term *ftg-function*, for the case $H^* = 1400$ and $d^* = 90$, are illustrated in Figure 22. Indeed, an increase in R_b^* yields a nearly uniform increase in the *ftg-function*, very close to the increase in R_b^*. More precisely, the simulations performed have shown that it is possible to find two dimensionless correction coefficients, $c_1(\tau^*)$ and $c_2(\tau^*)$, very close to 1, such that

$$\textit{ftg-function}\left(R_b^*, H^*, d^*, \tau^*\right) = \textit{ftg-function}\left(0.2, H^*, d^*, \tau^*\right) + c_1\left(\tau^*\right)\left(0.2 - R_b^*\right), \text{ for } R_b^* < 0.2 , \qquad (24)$$

$$\textit{ftg-function}\left(R_b^*, H^*, d^*, \tau^*\right) = \textit{ftg-function}\left(0.2, H^*, d^*, \tau^*\right) + c_2\left(\tau^*\right)\left(R_b^* - 0.2\right), \text{ for } R_b^* > 0.2 . \qquad (25)$$

The coefficients $c_1(\tau^*)$ and $c_2(\tau^*)$ evaluated for $H^* = 1400$ and $d^* = 90$ can be applied to all the fields with 2 BHEs considered, and the accuracy of Eqs. (24) and (25) is excellent for $0.1 \le R_b^* \le 0.3$. The accuracy of the approximate evaluation of the long-term *ftg-functions* through the coefficients $c_1(\tau^*)$ and $c_2(\tau^*)$, for a field of 2 BHEs with $H^* = 2000$ and $d^* = 60$, is illustrated in Figure 23, where the approximate *ftg-functions* for $R_b^* = 0.1$ and $R_b^* = 0.3$ evaluated from that for $R_b^* = 0.2$ are compared to those obtained by the direct simulations. The root-mean-square deviation between the approximate values and those obtained by direct simulations is 0.0002, for both $R_b^* = 0.1$ and $R_b^* = 0.3$.

Tables of the long-term *ftg-functions* of fields with 2 BHEs and isothermal fluid, with steps of 0.05 in $\log_{10}(\tau^*)$, are reported in the Excel file "Long-term *ftg-functions* for fields with 2 BHEs", available in the Repository AMSActa (see Data Availability Section). The same file reports also the values of the coefficients $c_1(\tau^*)$ and $c_2(\tau^*)$ for these fields.
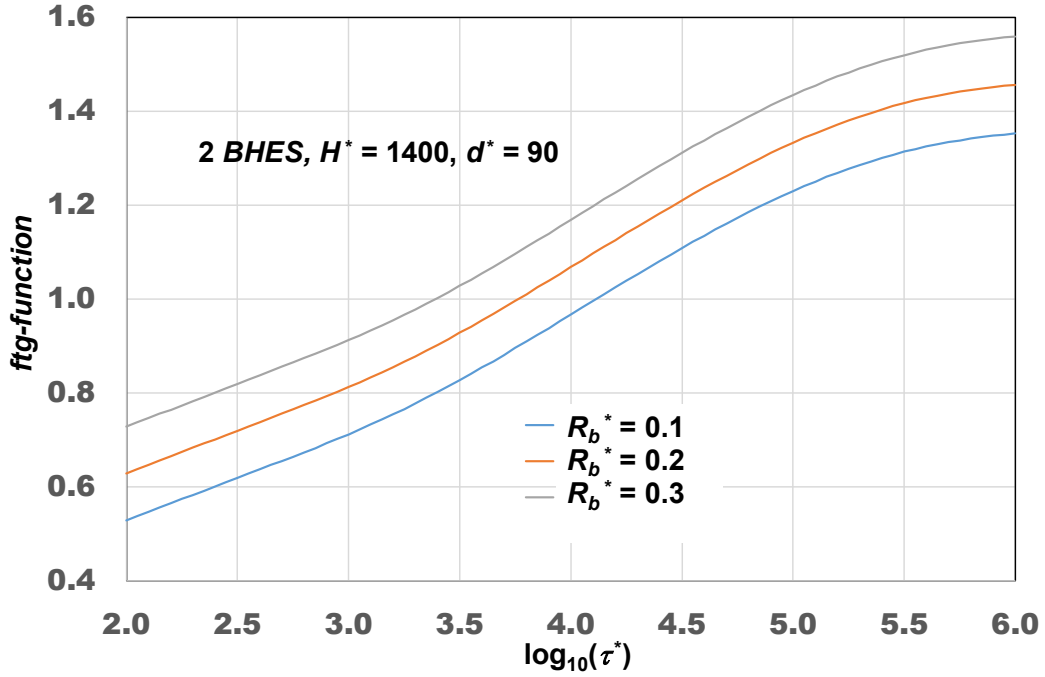
Figure 22. Effects of $R_b{}^*$ on the long-term *ftg-function* of a field with 2 BHEs, for $H^* = 1400$ and $d^* = 90$.
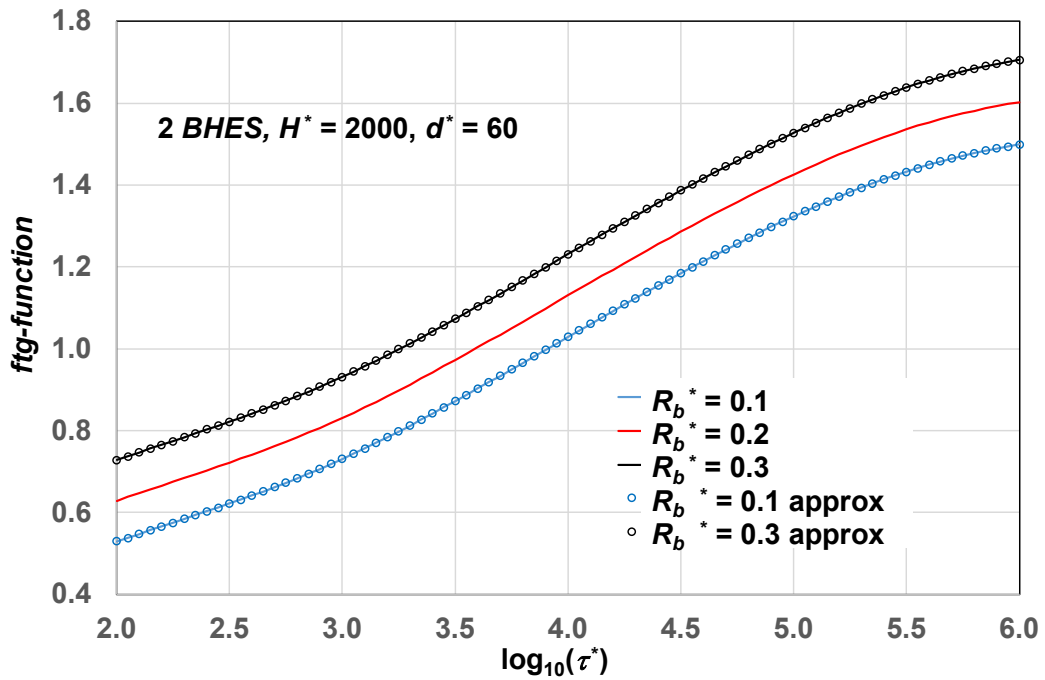

Figure 23. Approximate long-term *ftg-function*s for $R_b^* = 0.1$ and $R_b^* = 0.3$, for a field of 2 BHEs with $H^* = 2000$ and $d^* = 60$, compared with those obtained by direct simulations.

9. Long-term *ftg-functions* for a line of 3 BHEs with isothermal fluid

The long-term *ftg-functions* for a line of 3 BHEs with isothermal fluid have been determined by 3D finite-element simulations with the following values of the dimensionless parameters: $B_d{}^* = 24$; $R_b{}^* = 0.2$; $H^* = 800, 1400, 2000$; $d^* = 60, 90, 120$. Then, the dimensionless correction coefficients, $c_1(\tau^*)$ and $c_2(\tau^*)$, that yield the *ftg-functions* for $R_b{}^* \neq 0.2$, have been determined by 3D finite-element

simulations with $R_b{}^* = 0.1, 0.3$; $H^* = 1400$; $d^* = 90$. The use of the correction coefficients has allowed reducing the number of 3D simulations from 27 to 11.

For each geometric configuration, a computational domain where the ground is a rectangular parallelepiped centered in the axis of the central BHE has been employed, with dimensionless horizontal sides equal to $5000 + 2d^*$ along x, equal to 5000 along y, and equal to $(B_d{}^* + H^* + 2500)/a$ along z, where a is the rescaling coefficient in the vertical direction. To reduce the computation time for the highest values of H^*, the coefficient a has been assumed equal to 20 for $H^* = 800$, equal to 25 for $H^* = 1400$ and for $H^* = 2000$. Each BHE is modeled as in the previous sections.

To obtain equal fluid temperatures in the BHEs, the superconductive cylinders representing the fluid are interconnected with a superconductive horizontal bar with the same cross section and the same dimensionless thermal properties as in Section 8. A particular of the computational domain, centered in the upper part of central BHE, is illustrated in Figure 24. The figure refers to the geometry with $H^* = 1400$ and $d^* = 90$, where the employed mesh consists of 11 929 600 tetrahedral elements. The part of the figure in black and gray evidences the vertical superconductive elements that connect the solid representing water to the horizontal bar.
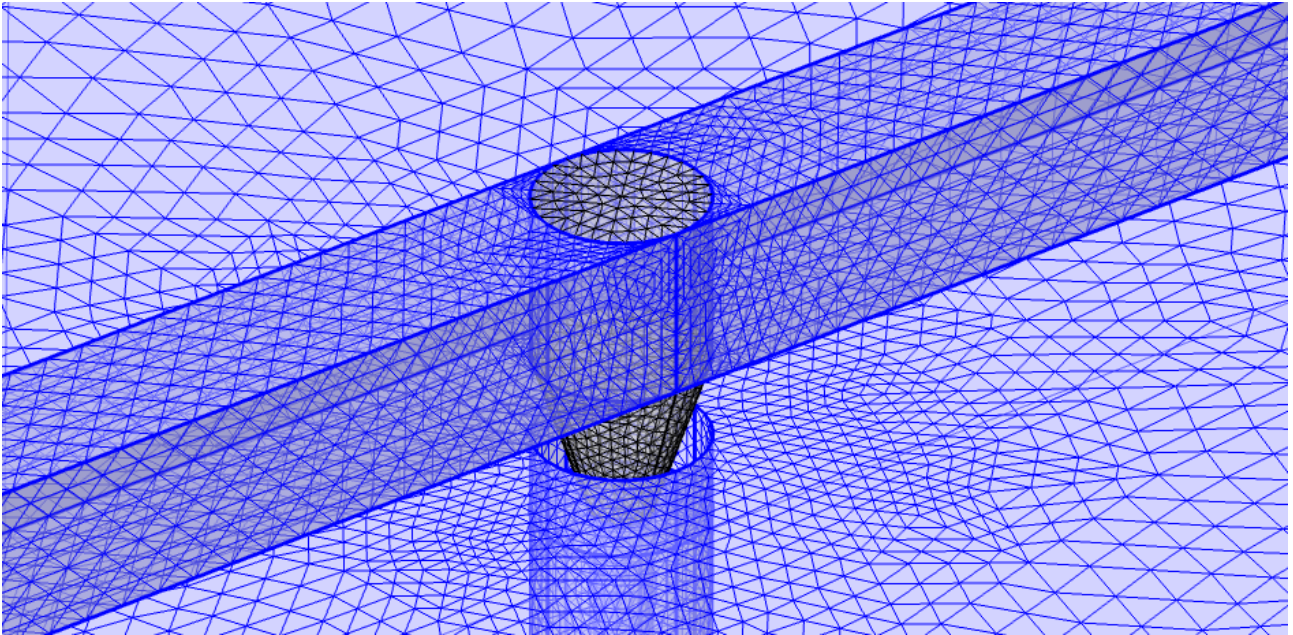

Figure 24. Particular of the computational domain and mesh employed for the simulation of the fields with 3 BHEs, $H^* = 1400$ and $d^* = 90$: connection of the central BHE to the superconductive bar.

Before performing the final computations for the lines of 3 BHEs, the 3D simulation code has been validated by comparing the long-term *g-function* yielded by the code with that obtained by integrating the semi-analytical expression of the length-averaged temperature on a surface with radius r determined by Claesson and Javed [6] through the FLS model with uniform linear heat flux:

$$T_m(r,\tau) - T_g = \frac{q_l}{4\pi k_g} \int\limits_{1/\sqrt{4\frac{k_g}{(\rho c)_g}\tau}}^{\infty} e^{-r^2 s^2} \frac{\mathrm{I_{LS}}(H\,s, B_d\,s)}{H\,s^2}\,\mathrm{d}s \quad, \tag{26}$$

$$\mathrm{I_{LS}}(h,d) = 2\times\mathrm{Ierf}(h) + 2\times\mathrm{Ierf}(h+2d) - \mathrm{Ierf}(2h+2d) - \mathrm{Ierf}(2d) \quad, \tag{27}$$

$$\mathrm{Ierf}(x) = x\,\mathrm{Erf}(x) - \frac{1-e^{-x^2}}{\sqrt{\pi}} \quad, \tag{28}$$

$$\mathrm{Erf}(x) = \frac{2}{\sqrt{\pi}} \int_0^x e^{-t^2}\,\mathrm{d}t \quad. \tag{29}$$

The validation has been performed for the case $H^* = 1400$, $d^* = 90$, and $R_b{}^* = 0.2$. To obtain the condition of uniform linear heat flux in the simulation code, the thermal conductivity $k_{sc}{}^* = 0$ for the solid material (formerly superconductor) that interconnects the BHEs has been employed, together with the thermal conductivity $k_{sc}{}^* = 1$ for the solid (formerly superconductor) representing water. Moreover, the boundary condition of uniform heat flux imposed on the top of the superconductor has been replaced with an adiabatic condition, coupled with a uniform heat generation in the solid representing water. The simulations have been performed with three meshes: Mesh 1, obtained by a regular refinement of the extremely fine physics-controlled mesh build by the software and having 1 491 576 tetrahedral elements; Mesh 2, obtained by a regular refinement of Mesh 1 and having 11 932 608 tetrahedral elements; Mesh 3, obtained from Mesh 2 by a regular refinement of the portion of domain occupied by the BHEs and having 15 571 661 tetrahedral elements. The FLS *g-function* for the field has been obtained through the *g-functions* for a single BHE determined by Eqs. (25 – 28) and the superposition of effects in space. The comparison, illustrated in Figure 25, shows a very good agreement between the long-term FLS *g-function* and that obtained through the simulation with Mesh 3: the root-mean-square deviation is 0.0041 and corresponds to 0.43% of the mean value of the long-term *g-function*.

The final simulations to obtain the *ftg-functions* for a line of 3 BHEs with isothermal fluid have been performed by Mesh 2, obtained by two regular refinements of the extremely fine physics-controlled mesh build by the software, after checking that the difference between the results obtained by Mesh 2 and those obtained by Mesh 3 is negligible when the dimensionless thermal conductivity of the superconductor is $k_{sc}{}^* = 10^9$, the heat flux is applied to the upper surface of the horizontal bar, and no heat generation occurs in the solid representing water. The relative and the absolute accuracy have been set equal to 0.0001. The *ftg-functions* obtained by Mesh 1, Mesh 2, and Mesh 3, in the case $H^* = 1400$, $d^* = 90$, and $R_b{}^* = 0.2$, are illustrated in Figure 26. The figure shows that the *ftg-function* obtained by Mesh 3 is graphically indistinguishable from that obtained by Mesh 2.
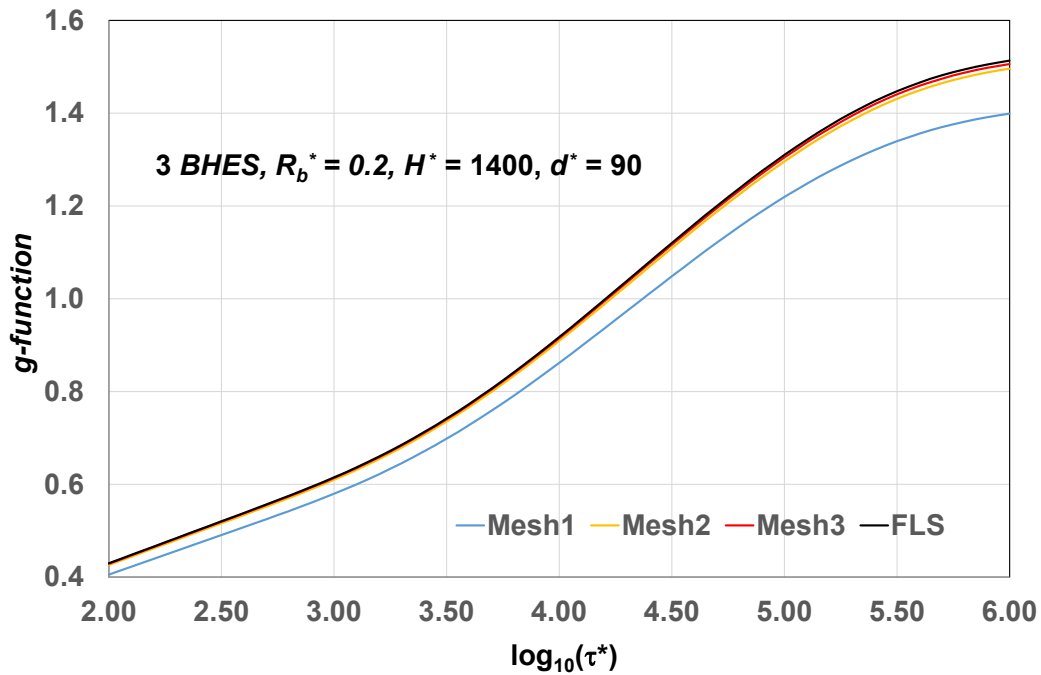
Figure 25. Comparison between the long-term *g-functions* obtained by 3D simulations and that obtained by the FLS solution [6], for a line of 3 BHEs with $H^* = 1400$, $d^* = 90$, and $R_b^* = 0.2$, subjected to a uniform linear heat flux.
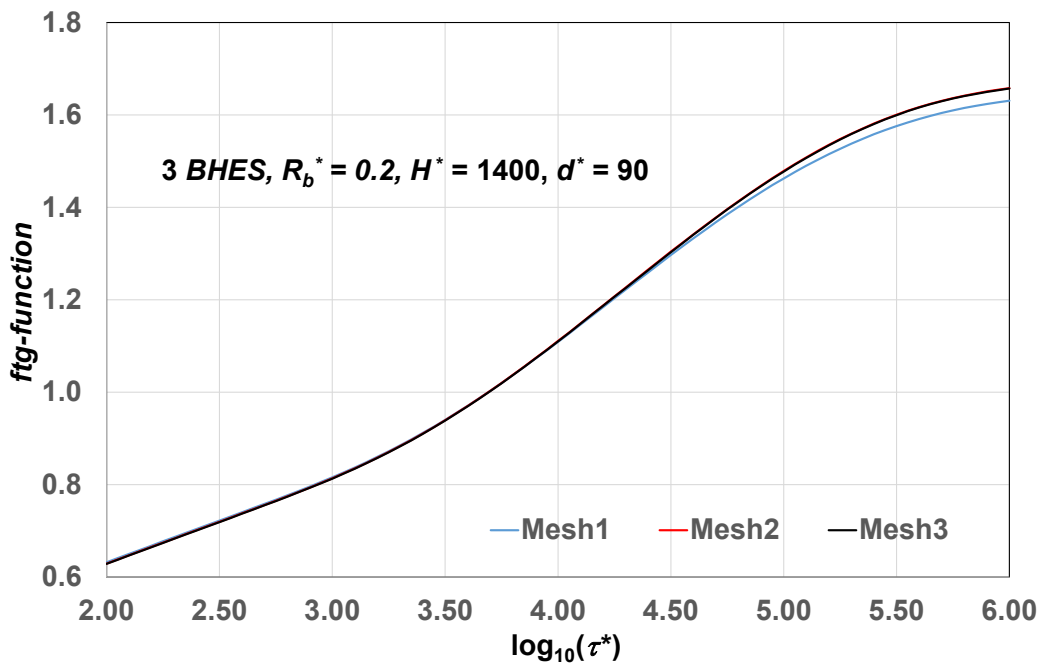

Figure 26. Comparison between the long-term *ftg-functions* with isothermal fluid, obtained by 3D simulations with Mesh 1, Mesh 2, and Mesh 3, for a line of three BHEs with $H^* = 1400$, $d^* = 90$, and $R_b^* = 0.2$.

Tables of the long-term *ftg-functions* of single-line fields with 3 BHEs and isothermal fluid, with steps of 0.05 in $\log_{10}(\tau^*)$, are reported in the Excel file "Long-term *ftg-functions* for single-line fields

with 3 BHEs", available in the Repository AMSActa (see Data Availability Section). The same file reports also the values of the coefficients $c_1(\tau^*)$ and $c_2(\tau^*)$ for these fields.

10. Long-term *ftg-functions* for a line of 4 BHEs with isothermal fluid

The long-term *ftg-functions* and the correction factors $c_1(\tau^*)$ and $c_2(\tau^*)$ for a line of 4 BHEs with isothermal fluid have been determined by 3D finite-element simulations with the same values of the dimensionless parameters B_d^*, R_b^*, H^*, and d^* as those employed in Section 9, the same kind of mesh, denoted by Mesh 2, and the same accuracy parameters, both equal to 0.0001.

For each geometric configuration, a computational domain with a symmetry plane placed between the second and the third BHE has been employed. In this domain, the ground is a rectangular parallelepiped with dimensionless horizontal sides equal to $2500 + 1.5\,d^*$ along x, equal to 5000 along y, and equal to $(B_d^* + H^* + 2500)/a$ along z, where a is the rescaling coefficient in the vertical direction, equal to 20 for $H^* = 800$ and equal to 25 for $H^* = 1400$ and for $H^* = 2000$. Each BHE is modeled as in the previous sections. The superconductive cylinders representing the fluid are interconnected with a superconductive horizontal bar and superconductive vertical elements, with the same geometry and the same dimensionless thermal properties as in Section 9, apart from the length of the horizontal bar. Figure 27 illustrates a particular of the computational domain for the geometry with $H^* = 1400$ and $d^* = 90$, where the employed mesh consists of 11 929 600 tetrahedral elements.
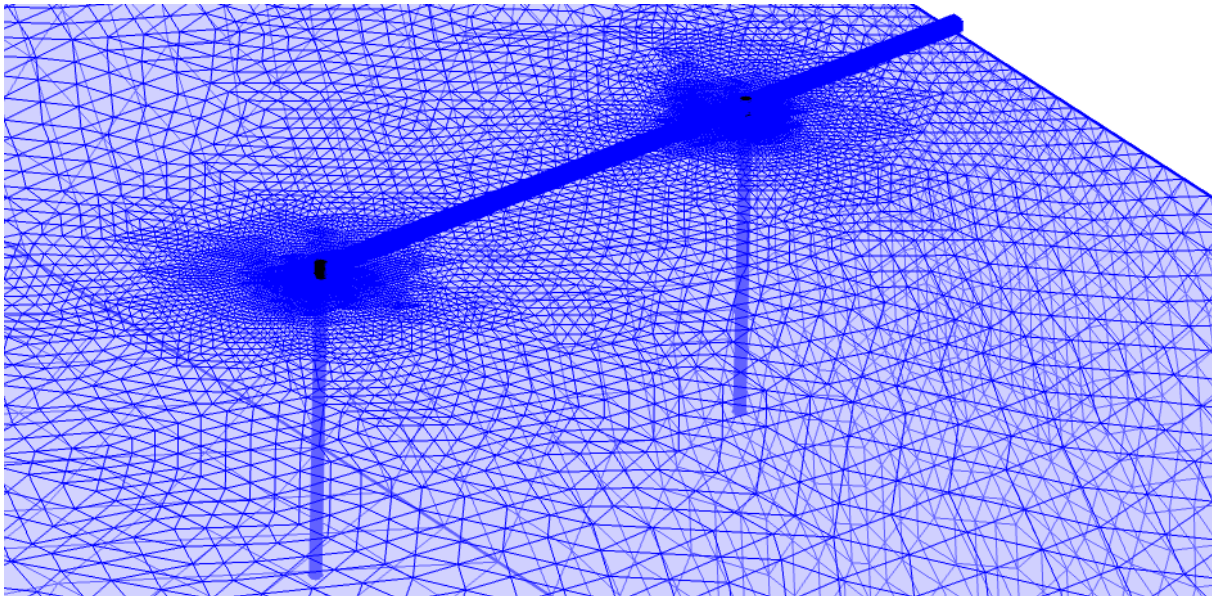

Figure 27. Particular of the computational domain and mesh (Mesh 2) employed for the simulation of the field with 4 BHEs, $H^* = 1400$, $d^* = 90$, $R_b^* = 0.2$.

Before performing the final computations for the lines of 4 BHEs, the 3D simulation code has been validated by comparing the long-term *g-function* yielded by the code with that obtained through the

semi-analytical solution of the FLS model determined by Claesson and Javed [6] and the superposition of effects in space. As in Section 9, the superconductor connecting the BHEs has been replaced by a solid with vanishing thermal conductivity and very low heat capacity, and the uniform heat flux imposed on the top of the horizontal bar has been replaced by a uniform generation term in the solid representing water, having dimensionless thermal conductivity $k_{sc}^* = 1$. The validation has been performed for the case $H^* = 1400$, $d^* = 90$, and $R_b^* = 0.2$, with Mesh1, Mesh 2 and Mesh 3, having 997104, 7976832 and 10420634 tetrahedral elements, respectively. The results of the validation are illustrated in Figure 28. The figure shows a very good agreement between the long-term *g-function* obtained by the simulation with Mesh 3 and that obtained by the FLS solution: the root mean square deviation is 0.00497 and corresponds to 0.49% of the mean value of the long-term *g-function*. The final simulations to obtain the *ftg-functions* for a line of 4 BHEs with isothermal fluid have been performed by Mesh 2, after checking that the difference between the results obtained by Mesh 2 and those obtained by Mesh 3 is negligible in this case.
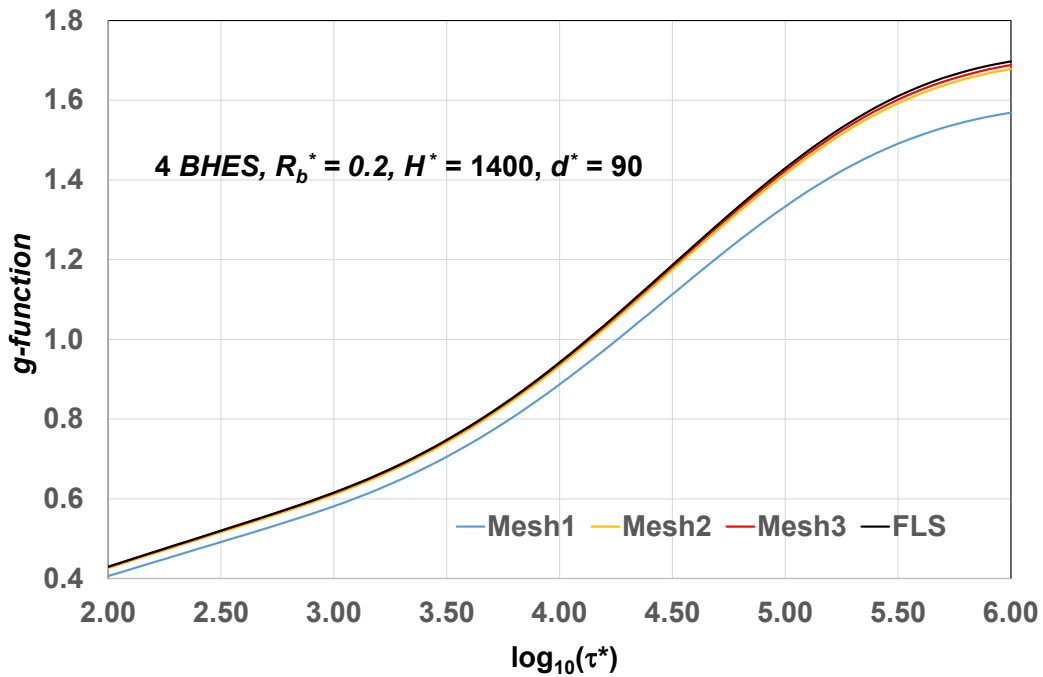

Figure 28. Comparison between the long-term *g-functions* obtained by 3D simulations and that obtained by the FLS solution [6], for a line of 4 BHEs with $H^* = 1400$, $d^* = 90$, and $R_b^* = 0.2$, subjected to a uniform linear heat flux.

Tables of the long-term *ftg-functions* of single-line fields with 4 BHEs and isothermal fluid, with steps of 0.05 in $\log_{10}(\tau^*)$, are reported in the Excel file "Long-term *ftg-functions* for single-line fields with 4 BHEs", available in the Repository AMSActa (see Data Availability Section). The same file reports also the values of the coefficients $c_1(\tau^*)$ and $c_2(\tau^*)$ for these fields.

The long-term *ftg-functions* obtained for a single BHE, a line of 2 BHEs, a line of 3 BHEs and a line of 4 BHEs with isothermal fluid, with the most typical values of H^*, d^* and R_b^*, namely $H^* = 1400$, $d^* = 90$, and $R_b^* = 0.2$, are reported in Figure 29, and are compared with the *ftg-functions* yielded by the FLS solution with uniform heat flux [6], obtained by adding R_b^* to the *g-functions*. The comparison between the *ftg-functions* for different numbers of BHEs shows that the effects of the thermal interference between BHEs are relevant in the long term, even for a line of few BHEs with a typical length (105 m for BHE radius 7.5 cm) and a rather wide separation (6.75 m for BHE radius 7.5 cm). The comparison between the *ftg-functions* corresponding to different working conditions, namely isothermal fluid and uniform heat flux, shows that the overestimation of the *ftg-functions* due to the assumption of uniform heat flux is negligible for a single BHE, but becomes significant for higher numbers of BHEs. For a line of 3 BHEs, the overestimation is equal to 2.10% for $\tau^* = 10^5$ and to 3.33% for $\tau^* = 10^6$. For a line of 4 BHEs, the overestimation is equal to 2.73% for $\tau^* = 10^5$ and to 4.46% for $\tau^* = 10^6$.
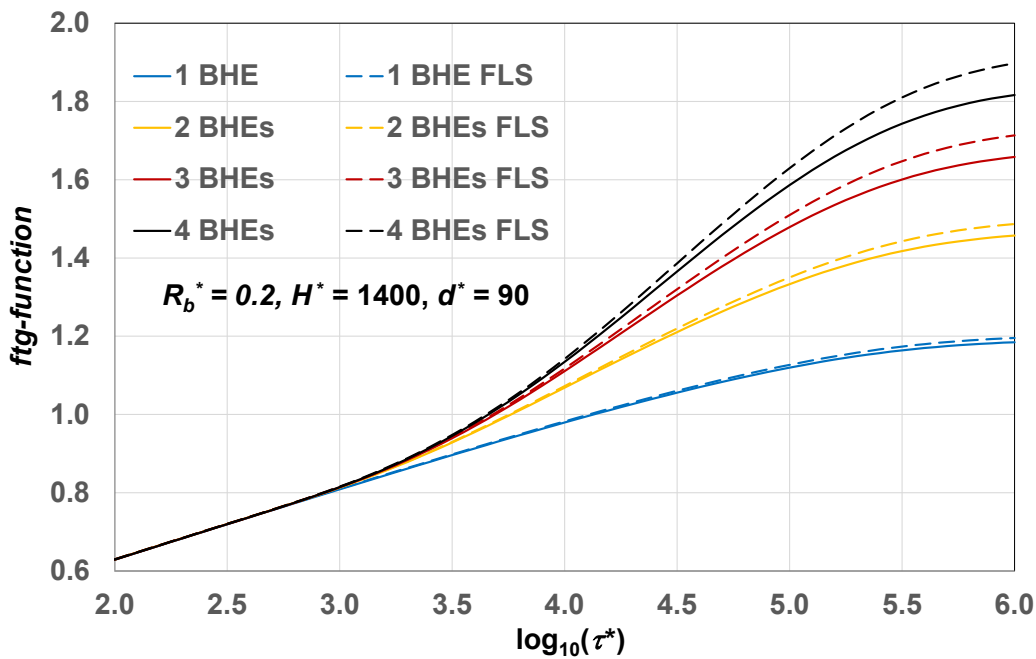

Figure 29. Long-term *ftg-functions* for a single BHE, a line of 2 BHEs, a line of 3 BHEs and a line of 4 BHEs, with isothermal fluid (solid lines), compared with those yielded by the FLS solution with uniform heat flux (dashed lines), for $H^* = 1400$, $d^* = 90$, and $R_b^* = 0.2$.

11. Interpolation method and examples

The short-term *ftg-functions* depend on R_b^*, r_{eq}^*, and $(\rho c)_{eq}^*$. The dependence on R_b^* can be considered as linear, but those on r_{eq}^* and on $(\rho c)_{eq}^*$ are nonlinear. Therefore, the following interpolation method between the results reported in our auxiliary material is recommended. Consider

two values of R_b^* that include the correct one. These values will be denoted here by R_{b1}^* and R_{b2}^*. Select R_{b1}^* and $r_{eq}^* = 0.2$, and perform a second-order interpolation between the corresponding three columns of $(\rho c)_{eq}^*$, to determine a column with R_{b1}^*, $r_{eq}^* = 0.2$, and the correct value of $(\rho c)_{eq}^*$. Repeat the second-order interpolation with $r_{eq}^* = 0.35$, and with $r_{eq}^* = 0.5$. You will obtain three columns of results, with R_{b1}^* and the correct value of $(\rho c)_{eq}^*$. Perform a second order interpolation between these columns, by imposing the correct value of r_{eq}^*. You will obtain a column with R_{b1}^*, and with the correct values of $(\rho c)_{eq}^*$ and of r_{eq}^*. Repeat the procedure with R_{b2}^*, then perform a linear interpolation between the two columns of results obtained.

The long-term *ftg-functions* for a single BHE depend on R_b^* and H^*. The dependence on R_b^* is linear, but that on H^* is not. Consider two values of R_b^* that include the correct one, denoted by R_{b1}^* and R_{b2}^*. Select R_{b1}^*, and perform a second order interpolation between the columns with the different values of H^*, to obtain a column with R_{b1}^* and the correct value of H^*. Repeat the procedure with R_{b2}^*, then perform a linear interpolation between the two columns of results obtained.

The long-term *ftg-functions* for single-line bore fields with 2, 3, or 4 BHEs depend on R_b^*, H^* and d^*. The dependence on R_b^* can be determined by the correction coefficients $c_1(\tau^*)$ and $c_2(\tau^*)$. Select $R_b^* = 0.2$, $H^* = 800$, and perform a perform a second order interpolation between the columns with the different values of d^*, to obtain a column with $R_b^* = 0.2$, $H^* = 800$, and the correct value of d^*. Repeat the same procedure with $H^* = 1400$ and $H^* = 2000$, then perform a second order interpolation between the three columns obtained, to determine a column with the correct values of d^* and of H^*. Finally, apply the correction factor $c_1(\tau^*)$, if $R_b^* < 0.2$, or $c_2(\tau^*)$, if $R_b^* > 0.2$.

If one denotes by x_0, x_1, x_2 the values of a dimensionless parameter in three columns of results, by y_0, y_1, y_2 the corresponding values of the *ftg-function* at a given instant of time, by x the correct value of the dimensionless parameter, and by y the corresponding value of the *ftg-function* at that time, the second order interpolation is given by

$$y = y_0 + a\left(x - x_0\right)^2 + b\left(x - x_0\right) , \tag{30}$$

$$a = \frac{\left(y_1 - y_0\right)\left(x_2 - x_0\right) - \left(y_2 - y_0\right)\left(x_1 - x_0\right)}{\left(x_1 - x_0\right)^2\left(x_2 - x_0\right) - \left(x_2 - x_0\right)^2\left(x_1 - x_0\right)} , \tag{31}$$

$$b = \frac{y_2 - y_0}{x_2 - x_0} - a\left(x_2 - x_0\right) . \tag{32}$$

A check of the accuracy of the proposed interpolation method, in the case of one BHE with $R_b^* = 0.15$, $r_{eq}^* = 0.28$, $(\rho c)_{eq}^* = 0.85$, and $H^* = 1100$, is illustrated in Figure 30, where the *ftg-function* obtained by interpolation is compared with that obtained directly by a finite-element simulation similar to those performed to determine the tables of the *ftg-functions*. The figure shows that the interpolation

accuracy is excellent. The root-mean-square deviation between the interpolated values and those computed directly is 0.0011.

Another check, regarding the long-term *ftg-function* of a single-line field of 4 BHEs with $R_b{}^* = 0.25$, $H^* = 1700$, $d^* = 110$, is illustrated in Figure 31. The figure shows that the interpolation accuracy is good. The root-mean-square deviation between the interpolated values and those computed directly is 0.0060.

Two Excel files that perform automatically the interpolations are available in the Repository AMSActa (see Data Availability Section). The first file ("Interpolation short term") yields the short-term *ftg-function* for any set of values of $R_b{}^*$, $r_{eq}{}^*$, and $(\rho c)_{eq}{}^*$. The second one ("Interpolation long term 1-2-3-4 BHEs") yields the long-term *ftg-function* for any single-line bore field with up to 4 BHEs and any set of values of $R_b{}^*$, H^* and d^*.
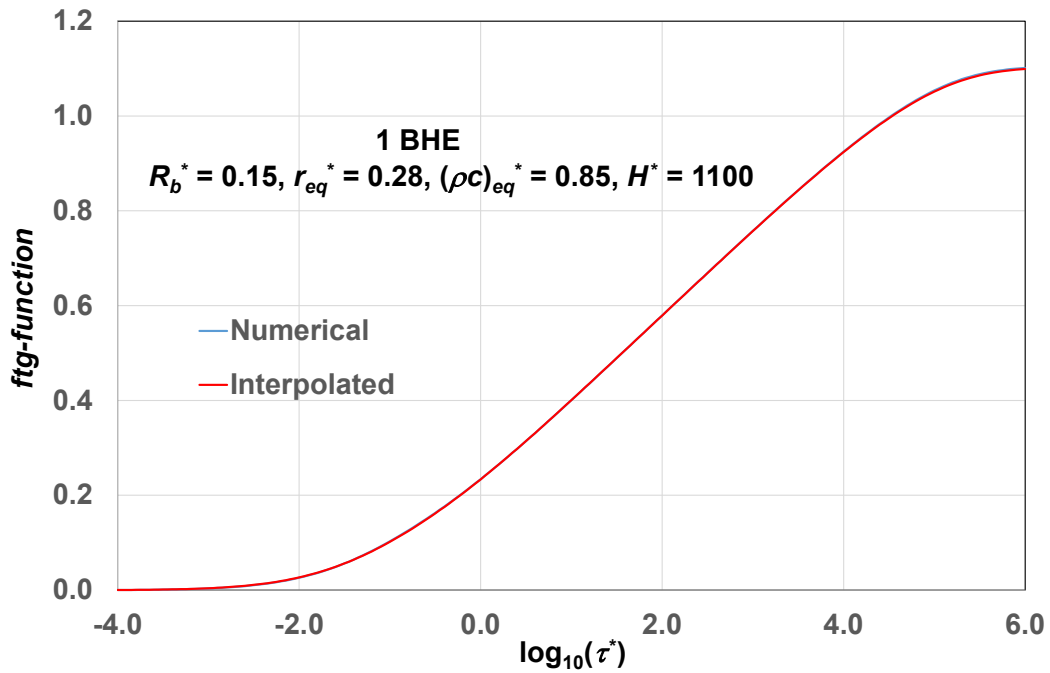

Figure 30. *Ftg-function* for a single BHE with $R_b{}^* = 0.15$, $H^* = 1100$, $r_{eq}{}^* = 0.28$, and $(\rho c)_{eq}{}^* = 0.85$, obtained by a finite-element simulation and by interpolation.
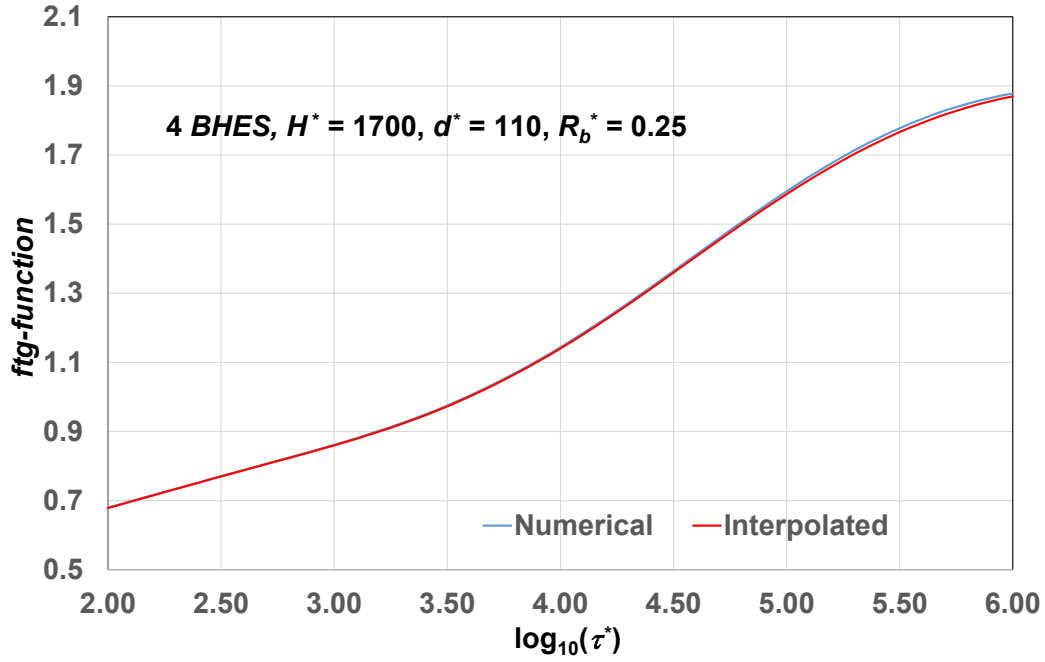
Figure 31. *Long-term ftg-function* for a field of 4 BHEs with $H^* = 1700$, $d^* = 110$, and $R_b{}^* = 0.25$, obtained by a finite-element simulation and by interpolation.

12. Conclusions

Very accurate tables of dimensionless fluid-to-ground thermal response factors, denoted by *ftg-functions*, have been provided. By suitable interpolations, these tables allow determining the time evolution of the mean fluid temperature of any single-line bore field with up to four BHEs subjected to a given time-constant heat load. The working condition considered, namely that of isothermal fluid, is very close to the real condition of BHEs fed in parallel with the same inlet temperature. The tables are presented as columns of Excel files, where each column corresponds to fixed values of some dimensionless parameters. To reduce the number of combinations of the parameters, the *ftg-functions* have been divided into short-term *ftg-functions*, that hold for values of the dimensionless time $\tau^* \leq \tau_0{}^* = 10^2$, and long-term *ftg-functions*, that hold for $\tau^* \geq \tau_0{}^*$. The interval of dimensionless time considered is $10^{-4} \leq \tau^* \leq 10^6$. For a ground with thermal diffusivity equal to 7.5×10^{-7} m^2/s and a BHE radius $r_b = 7.5$ cm, $\tau_0{}^*$ corresponds to a time $\tau = 7.5 \times 10^5$ s ≈ 208.33 h, and the range of τ^* considered corresponds to 0.75 s $\leq \tau \leq 7.5 \times 10^9$ s ≈ 237.8 years.

The results have been obtained by finite-element simulations implemented in COMSOL Multiphysics, where each BHE is modeled as a one-material cylindrical annulus with the same external radius as the BHE, containing a superconductive inner core with radius r_{eq} and the same volumetric heat capacity as the annulus. The thermal conductivity of the cylindrical annulus and the

volumetric heat capacity of both the inner core and the annulus are such that the thermal resistance of the annulus is equal to the BHE thermal resistance, R_b, and the heat capacity of the cylindrical model is equal to that of the BHE. For fields with more than one BHE, the BHEs are thermally interconnected by a superconductive bar, that is subjected to the total heat flux.

The short-term *ftg-functions* are independent of the number of BHEs, and have been provided as functions of the dimensionless BHE thermal resistance, $R_b{}^*$, of the dimensionless radius of the superconductive core, $r_{eq}{}^*$, and of the dimensionless volumetric heat capacity of the materials of the model, $(\rho c)_{eq}{}^*$. The long-term *ftg-functions* have been provided, for each bore field, as functions of the dimensionless BHE thermal resistance, $R_b{}^*$, of the dimensionless BHE length, H^*, and, for fields with two or more BHEs, of the dimensionless distance between the BHEs, d^*. The dimensionless buried depth of the BHEs has been fixed, equal to 24; for a BHE radius $r_b = 7.5$ cm it corresponds to 1.8 m, a typical value for temperate climates.

Each simulation has been performed for the whole interval of dimensionless time. Then, both the short-term and the long-term *ftg-functions* have been slightly modified in a neighborhood of $\tau_0{}^*$, to obtain short-term *ftg-functions* and long-term *ftg-functions* that depend only on $R_b{}^*$ at $\tau_0{}^*$. The corrections changed only the fourth decimal digit or, exceptionally, also the third decimal digit by one unit.

A precise interpolation method between the columns of the given *ftg-functions* has been suggested and checked. Two Excel files that perform automatically the interpolations, for the short-term and the long-term *ftg-functions* respectively, have also been provided. After entering the dimensionless parameters that characterize any single-line BHE field with up to 4 BHEs, these files instantly yield a short-term and a long-term *ftg-function* perfectly joined at the separation instant, and can be exploited easily for the design of single-line BHE fields.

The results have shown that the use of the FLS solution with uniform wall heat flux yields an overestimation of the *ftg-functions* that is negligible for a single BHE, but becomes significant for higher numbers of BHEs. For a line of 4 BHEs with $H^* = 1400$ and $d^* = 90$, the overestimation is equal to 2.73% for $\tau^* = 10^5$ and to 4.46% for $\tau^* = 10^6$.

The main novelties of the study are the characterization of each BHE field by a few dimensionless parameters, the improvement of the BHE model presented in Ref. [30], the usefulness, the accuracy, and the speed and simplicity of use of the final results.

The accuracy of the code employed for the single BHE, and of those employed for the fields with 3 and 4 BHEs, has been checked by comparison with analytical solutions, through slight modifications of the codes in order to reproduce the analytical conditions. The comparisons yielded root-mean-square deviations equal to 0.023%, 0.43%, and 0.49% of the mean value, respectively for 1, 3 and 4

BHEs. The accuracy of the code employed for the field with 2 BHEs has been checked by comparison with the long-term *ftg-function* obtained for a single BHE, in the limit of an extremely high distance between the BHEs. The comparison yielded a root mean square deviation equal to 0.054% of the mean value.

The results apply to single U-tube and double U-tube BHEs, with ratios between length and radius from 800 and 2000, i.e., length between 60 and 150 m for r_b =7.5 cm, in the absence of appreciable effects of groundwater seepage. The extension of the results to cases with considerable effects of groundwater seepage and to other BHE-field geometries will be considered in future work.

Data Availability

Acknowledgment

References

1. Jung, Y.-J.; Kim, H.-J.; Choi, B.-E.; Jo, J.-H.; Cho, Y.-H. A Study on the Efficiency Improvement of Multi-Geothermal Heat Pump Systems in Korea Using Coefficient of Performance. *Energies* **2016**, *9*, 356. https://doi.org/10.3390/en9050356

2. Rivoire, M.; Casasso, A.; Piga, B.; Sethi, R. Assessment of Energetic, Economic and Environmental Performance of Ground-Coupled Heat Pumps. *Energies* **2018**, *11*, 1941. https://doi.org/10.3390/en11081941

3. Zeng, H.Y.; Diao, N.R.; Fang, Z.H. A finite line-source model for boreholes in geothermal heat exchangers. *Heat Transfer–Asian Research* **2002**, *31*, 558–567. https://doi.org/10.1002/htj.10057

4. Lamarche, L.; Beauchamp, B. A new contribution to the finite line-source model for geothermal boreholes. *Energ Buildings* **2007**, *39*, 188–198. https://doi.org/10.1016/j.enbuild.2006.06.003

5. Bandos, T.V.; Montero, A.; Fernandez, E.; Santander, J.L.G.; Isidro, J.M.; Perez, J.; Fernandez de Cordoba, P.J.; Urchueguía, J.F. Finite line-source model for borehole heat exchangers: effect

of vertical temperature variations. *Geothermics* **2009**, *38*, 263–270. https://doi.org/10.1016/j.geothermics.2009.01.003

6. Claesson, J.; Javed, S. An analytical method to calculate borehole fluid temperatures for time-scales from minutes to decades. *ASHRAE Tran* **2011**, *117 (2)*, 279–288.

7. Eskilson, P. Thermal analysis of heat extraction boreholes, Ph.D. Thesis, University of Lund, Lund, Sweden, 1987.

8. Cimmino, M.; Bernier, M. A semi-analytical method to generate g-functions for geothermal bore fields. *Int J Heat Mass Tran* 2014, 70, 641–650. https://doi.org/10.1016/j.ijheatmasstransfer.2013.11.037

9. Lamarche, L. G-function generation using a piecewise-linear profile applied to ground heat exchangers. Int. J. Heat Mass Transfer **2017**, 115, 354–360. https://doi.org/10.1016/j.ijheatmasstransfer.2017.08.051

10. Cimmino, M. Fast calculation of the g-functions of geothermal borehole fields using similarities in the evaluation of the finite line source solution. J. Build. Perform. Simul. **2018**, 11, 655-668. https://doi.org/10.1080/19401493.2017.1423390.

11. Monzó, P.; Mogensen, P.; Acuña, J.; Ruiz-Calvo, F.; Montagud, C. A novel numerical approach for imposing a temperature boundary condition at the borehole wall in borehole fields. *Geothermics* **2015**, *56*, 35–44. https://doi.org/10.1016/j.geothermics.2015.03.003

12. Naldi, C.; Zanchini, E. A new numerical method to determine isothermal g-functions of borehole heat exchanger fields. *Geothermics* **2019**, *77*, 278–287. https://doi.org/10.1016/j.geothermics.2018.10.007

13. Monzó, P.; Puttige, A.R.; Acuña, J.; Mogensen, P.; Cazorla, A.; Rodriguez, J.; Montagud, C.; Cerdeira, F. Numerical modeling of ground thermal response with borehole heat exchangers connected in parallel. *Energ Buildings* **2018**, *172*, 371–384. https://doi.org/10.1016/j.enbuild.2018.04.057

14. Cimmino, M. The effects of borehole thermal resistances and fluid flow rate on the g-functions of geothermal bore fields. *Int J Heat Mass Tran* **2015**, *91*, 1119–1127. https://doi.org/10.1016/j.ijheatmasstransfer.2015.08.041

15. De Carli, M.; Tonon, M.; Zarrella, A.; Zecchin, R. A computational capacity resistance model (CaRM) for vertical ground-coupled heat exchangers. *Renew Energ* **2010**, *35*, 1537–1550. https://doi.org/10.1016/j.renene.2009.11.034

16. Zarrella, A.; Scarpa, M.; De Carli, M. Short time step analysis of vertical ground-coupled heat exchangers: The approach of CaRM. *Renew Energ* **2011**, *36*, 2357–2367. https://doi.org/10.1016/j.renene.2011.01.032

17. Bauer, D.; Heidemann, W.; Muller-Steinhagen, H.; Diersch, H.-J.G. Thermal resistance and capacity models for borehole heat exchangers. *Int J Energ Res* **2011**, *35*, 312–320. https://doi.org/10.1002/er.1689

18. Pasquier, P.; Marcotte, D. Short-term simulation of ground heat exchanger with an improved TRCM. *Renew Energ* **2012**, *46*, 92–99. https://doi.org/10.1016/j.renene.2012.03.014

19. Ruiz-Calvo, F.; De Rosa, M.; Acuña, J.; Corberán, J.M.; Montagud, C. Experimental validation of a short-term Borehole-to-Ground (B2G) dynamic model. *Appl Energ* **2015**, *140*, 210–223. https://doi.org/10.1016/j.apenergy.2014.12.002

20. Gu, Y., O'Neal, D.L. Development of an equivalent diameter expression for vertical U-tubes used in ground-coupled heat pumps. ASHRAE Transactions **1998**, *104*, 347–355.

21. Shonder, J.A., Beck, J.V. Determining effective soil formation thermal properties from field data using a parameter estimation technique. ASHRAE Transactions **1999**, *105* (1), 458–466.

22. Beier, R.A., Smith, M.D. Minimum duration of in-situ tests on vertical boreholes. ASHRAE Transactions **2003**, *109* (2), 475–486.

23. Xu, X.; Spitler, J.D. Modeling of vertical ground loop heat exchangers with variable convective resistance and thermal mass of the fluid. In Proceedings of the 10th International Conference on Thermal Energy Storage, Ecostock 2006, Pomona, New Jersey, USA, 2006.

24. Lamarche, L.; Beauchamp, B. New solutions for the short-time analysis of geothermal vertical boreholes. *Int J Heat Mass Tran* **2007**, *50*, 1408–1419. https://doi.org/10.1016/j.ijheatmasstransfer.2006.09.007

25. Bandyopadhyay, G., Kulkarni, M., Mann, M. A new approach to modeling ground heat exchangers in the initial phase of heat flux build-up. ASHRAE Transactions **2008**, *114* (2), 428–439.

26. Bandyopadhyay, G., Gosnold, W., Mann, M. Analytical and semi-analytical solutions for short-time transient response of ground heat exchangers. Energy and Buildings **2008**, *40*, 1816–1824. https://doi.org/10.1016/j.enbuild.2008.04.005

27. Man, Y.; Yang, H.; Diao, N.; Liu, J.; Fang, Z. A new model and analytical solutions for borehole and pile ground heat exchangers. *Int J Heat Mass Tran* **2010**, *53*, 2593–2601. https://doi.org/10.1016/j.ijheatmasstransfer.2010.03.001

28. Javed, S.; Claesson, J. New analytical and numerical solutions for the short-term analysis of vertical ground heat exchangers. *ASHRAE Tran* **2011**, *117 (1)*, 3–12.

29. Lamarche, L. Short-time analysis of vertical boreholes, new analytic solutions and choice of equivalent radius. *Int J Heat Mass Tran* **2015**, *91*, 800–807. https://doi.org/10.1016/j.ijheatmasstransfer.2015.07.135

30. Naldi, C.; Zanchini, E. A one-material cylindrical model to determine short- and long-term fluid-to-ground response factors of single U-tube borehole heat exchangers. *Geothermics* **2020**, *86*, 101811. https://doi.org/10.1016/j.geothermics.2020.101811

31. Naldi, C.; Zanchini, E. Full-Time-Scale Fluid-to-Ground Thermal Response of a Borefield with Uniform Fluid Temperature. *Energies* **2019**, *12*, 3750. https://doi.org/10.3390/en12193750

32. Laferrière, A.; Cimmino, M.; Picard, D.; Helsen, L. Development and validation of a full-time-scale semi-analytical model for the short- and long-term simulation of vertical geothermal bore fields. *Geothermics* **2020**, *86*, 101788. https://doi.org/10.1016/j.geothermics.2019.101788

33. Lee, C.K. Effects of multiple ground layers on thermal response test analysis and ground-source heat pump simulation. *Applied Energy* **2011**, *88*, 4405–4410. https://doi.org/10.1016/j.apenergy.2011.05.023

34. Luo, J.; Rohn, J.; Bayer, M.; Priess, A.; Xiang, W. Analysis on performance of borehole heat exchanger in a layered subsurface, *Applied Energy* **2014**, *123*, 55–65. https://doi.org/10.1016/j.apenergy.2014.02.044

35. Zanchini, E.; Jahanbin, A. Effects of the temperature distribution on the thermal resistance of double U-tube borehole heat exchangers. Geothermics **2018**, *71*, 46–54. https://doi.org/10.1016/j.geothermics.2017.07.009

36. Jahanbin, A.; Naldi, C.; Zanchini, E. Relation between mean fluid temperature and outlet temperature for single U-tube boreholes. Energies **2020**, *13*, 828. https://doi.org/10.3390/en13040828

37. Zanchini, E.; Jahanbin, A. Simple equations to evaluate the mean fluid temperature of double-U-tube borehole heat exchangers. Appl. Energy **2018**, *231*, 320–330. https://doi.org/10.1016/j.apenergy.2018.09.094

38. Morchio, S.; Fossa, M.; Beier, R.A. Study on the best heat transfer rate in thermal response test experiments with coaxial and U-pipe borehole heat exchangers. Appl. Therm. Eng. **2022**, *200*, 117621. https://doi.org/10.1016/j.applthermaleng.2021.117621

39. Morchio, S.; Pasquier, P.; Fossa, M.; Beier, R.A. A spectral method aimed at explaining the role of the heat transfer rate when the Infinite Line Source model is applied to Thermal Response Test analyses. Geothermics **2023**, *111*, 102722. https://doi.org/10.1016/j.geothermics.2023.102722

40. Morchio, S.; Fossa, M. Modelling and validation of a new hybrid scheme for predicting the performance of U-pipe borehole heat exchangers during distributed thermal response test experiments. Appl. Therm. Eng. **2021**, *186*, 116514. https://doi.org/10.1016/j.applthermaleng.2020.116514

41. Naldi, C.; Jahanbin, A.; Zanchini, E. A New Estimate of Sand and Grout Thermal Properties in the Sandbox Experiment for Accurate Validations of Borehole Simulation Codes. *Energies* **2021**, *14*, 1149. https://doi.org/10.3390/en14041149

42. Churchill, S.W. Comprehensive correlating equations for heat, mass and momentum transfer in fully developed flow in smooth tubes. *Ind. Eng. Chem. Fundam.* **1977**, *16*, 109–116. https://doi.org/10.1021/i160061a021

43. NIST Chemistry WebBook. Available online: https://webbook.nist.gov/chemistry/fluid/

44. Zanchini, E.; Lazzari, S.; Priarone, A. Improving the thermal performance of coaxial borehole heat exchangers. *Energy* **2010**, *35*, 657–666. https://doi.org/10.1016/j.energy.2009.10.038